

High-energy neutrino flux from individual blazar flares

Foteini Oikonomou¹★, Kohta Murase^{2,3}, Paolo Padovani^{1,4},
Elisa Resconi⁵ and Peter Mészáros²

¹ *European Southern Observatory, Karl-Schwarzschild-Str. 2, D-85748 Garching bei München, Germany*

² *Department of Physics; Department of Astronomy & Astrophysics; Center for Particle & Gravitational Astrophysics, Institute for Gravitation and the Cosmos, Pennsylvania State University, University Park, PA 16802, USA*

³ *Center for Gravitational Physics, Yukawa Institute for Theoretical Physics, Kyoto University, Kyoto, Kyoto 606-8502, Japan*

⁴ *Associated to INAF - Osservatorio Astronomico di Roma, via Frascati 33, I-00040 Monteporzio Catone, Italy*

⁵ *Technische Universität München, Physik-Department, James-Frank-Str. 1, D-85748 Garching bei München, Germany*

Accepted XXX. Received YYY; in original form ZZZ

ABSTRACT

Motivated by the recently reported evidence of an association between a high-energy neutrino and a γ -ray flare from the blazar TXS 0506+056, we calculate the expected high-energy neutrino signal from past, individual flares, from twelve blazars, selected in declinations favourable for detection with IceCube. To keep the number of free parameters to a minimum, we mainly focus on BL Lac objects and assume the synchrotron self-Compton mechanism produces the bulk of the high-energy emission. We consider a broad range of the allowed parameter space for the efficiency of proton acceleration, the proton content of BL Lac jets, and the presence of external photon fields. To model the expected neutrino fluence we use simultaneous multi-wavelength observations. We find that in the absence of external photon fields and with jet proton luminosity normalised to match the observed production rate of ultra-high-energy cosmic rays, individual flaring sources produce a modest neutrino flux in IceCube, $N_{\nu_{\mu}, > 100 \text{ TeV}}^{\text{IC}, 10\text{yr}} \lesssim 10^{-3}$ muon neutrinos with energy exceeding 100 TeV, stacking ten years of flare periods selected in the $> 800 \text{ MeV}$ *Fermi* energy range, from each source. Under optimistic assumptions about the jet proton luminosity and in the presence of external photon fields, we find that the two most powerful sources in our sample, AO 0235+164, and OJ 287, would produce, in total, $N_{\nu_{\mu}, \text{all flares}, > 100 \text{ TeV}}^{\text{IC} \times 10, 10\text{yr}} \approx 3$ muon neutrinos during *Fermi* flaring periods, in future neutrino detectors with total instrumented volume \sim ten times larger than IceCube, or otherwise, constrain the proton luminosity of blazar jets.

Key words: high-energy neutrinos, BL Lacertae objects

1 INTRODUCTION

The IceCube South Pole Neutrino Observatory¹ first reported the observation of high-energy astrophysical neutrinos (IceCube Collaboration 2013a,b, 2014b) a few years ago. Most recently, the neutrino flux collected over 6 years with deposited energy up to about 2 PeV was reported in IceCube Collaboration (2017a), bringing the number of high-energy starting neutrino events detected to 82 and strengthening the significance ($> 6.5\sigma$) of the observation that they are incompatible with being of purely terrestrial origin. Many

scenarios have been put forward for the origin of the neutrinos (see e.g. Ahlers & Halzen 2018 for a comprehensive review), but none are statistically supported at the exclusion of all other models at present.

The IceCube Collaboration has recently reported the observation of a $\gtrsim 290 \text{ TeV}$ muon neutrino, IceCube-170922A, coincident with a ~ 6 -month-long γ -ray flare of the blazar TXS 0506+056 (IceCube Collaboration et al. 2018) at redshift $z = 0.3365$ (Paiano et al. 2018). The neutrino detection prompted electromagnetic follow-up of the event, and the blazar flare was detected by several instruments, including MAGIC at energies exceeding $> 100 \text{ GeV}$. The correlation of the neutrino with the flare of TXS 0506+056 is inconsistent with arising by chance at the $3\text{--}3.5\sigma$ level. An archival search revealed 13 ± 5 further, high-energy neutrinos

★ E-mail: foikonom@eso.org

¹ <http://icecube.wisc.edu>

in the direction of TXS 0506+056 during a 6-month period in 2014-2015 (IceCube Collaboration 2018). These events were not accompanied by a γ -ray flare. Such an accumulation of events is inconsistent with arising from a background fluctuation at the 3.5σ level.

Blazars are active galactic nuclei (AGN) hosting a strong relativistic jet, which is oriented at a small angle with respect to the line of sight (Urry & Padovani 1995). Based on their optical spectra, blazars are divided into two main sub-classes, namely BL Lacertae objects (BL Lacs) and Flat Spectrum Radio Quasars (FSRQs). FSRQs display broad, strong emission lines, while BL Lacs exhibit at most weak emission lines, or in many cases featureless optical spectra. According to the value of the frequency (in the source rest-frame) at which the synchrotron, i.e. low-energy, peak, ν_S , of the spectral energy distribution (SED) occurs, blazars are divided into Low ($\nu_S < 10^{14}$ Hz), Intermediate ($10^{14} < \nu_S < 10^{15}$ Hz) and High energy peaked ($\nu_S > 10^{15}$ Hz), referred to in short as LSP, ISP and HSP respectively (Padovani & Giommi 1995; Fermi-LAT Collaboration 2010a).

Blazars have long been discussed as some of the most likely sources of high-energy neutrinos and cosmic-rays (see Mannheim 1995; Halzen & Zas 1997; Atoyan & Dermer 2001; Mücke et al. 2003; Murase et al. 2012a; Dermer et al. 2012; Murase et al. 2014; Padovani & Resconi 2014; Dermer et al. 2014; Petropoulou et al. 2015; Padovani et al. 2016; Gao et al. 2017; Rodrigues et al. 2018, and references therein).

Observations of the diffuse, all-sky neutrino spectrum by IceCube have resulted in constraints on the time-averaged emission from γ -ray bright blazars as sources of high-energy neutrinos from analyses of the observed diffuse neutrino flux (IceCube Collaboration 2016b, 2017a), and stacking analyses (IceCube Collaboration 2017c,b), down to $\lesssim 10 - 30\%$ of the diffuse astrophysical flux observed by IceCube at $\lesssim 100$ TeV. Thus blazars are inconsistent with being the dominant sources of the observed IceCube neutrino flux, unless the faintest blazars produce a disproportionately large amount of the neutrinos (Palladino et al. 2019). Constraints on blazars as dominant sources of the diffuse neutrino intensity observed by IceCube are additionally imposed by the lack of multiplets in the IceCube data, often referred to as “clustering constraints” (Murase & Waxman 2016; IceCube Collaboration 2015, 2017b; Neronov & Semikoz 2018; Murase et al. 2018), which limits in a complementary way the blazar contribution to the diffuse IceCube flux (Yuan et al. 2019).

Despite these limits the brightest neutrino sources, could still be blazars, due to, for example beaming. Blazar flaring periods are ideal for the detection of high-energy neutrinos both observationally and theoretically. Experimentally, the short, well-defined time duration of a flare means a very reduced background rate. Theoretically, in many models of neutrino emission, it is natural for the neutrino-production efficiency to be doubly enhanced during flares because it is typically expected that the proton injection increases while at the same time the target photon field is in an enhanced state (see e.g. Murase et al. 2014; Tavacchio et al. 2014; Petropoulou et al. 2016; Murase & Waxman 2016; Righi et al. 2017; Rodrigues et al. 2018). It was shown in Murase et al. (2018) that even though blazars emit

a small fraction of their γ -ray luminosity during flares (e.g. Fermi-LAT Collaboration 2010b, 2011), the distribution of flaring states of several studied *Fermi* blazars is consistent with neutrino production during flares being dominant in canonical models of neutrino emission.

The reported association of IceCube-170922A with, and flaring activity by, TXS 0506+056 (IceCube Collaboration et al. 2018; MAGIC Collaboration 2018; VERITAS Collaboration 2018; Keivani et al. 2018; Padovani et al. 2018) prompts us to investigate here the number of expected neutrino events from earlier blazar flares, that were also detectable by IceCube. Our aim is to investigate what are the conditions under which a blazar flare may produce a strong neutrino flux and to present a strategy for searching for neutrinos from blazar flares. The procedure we provide is easily applicable to general stacking analyses on blazar flares as we illustrate in the following sections.

The detectability of individual blazar flares of neutrinos in IceCube has been discussed in Atoyan & Dermer (2001); Halzen & Hooper (2005); Dermer et al. (2012, 2014); Petropoulou et al. (2016); Halzen & Kheirandish (2016); Kadler et al. (2016); Gao et al. (2017); Guepin & Kotera (2017). In Turley et al. (2016, 2018) IceCube data were analysed to look for neutrino emission spatially and temporally correlated with TeV emitting blazars, and *Fermi* data respectively. Here, we opt for a fully self-consistent, “leptonic” setup (referred to by other authors as “leptohadronic” or “hybrid”), in which the neutrinos are produced by the interactions of protons with target radiation fields in the source environment. In this context, leptonic refers to the fact that the majority of the observed γ -rays are produced by the interactions of leptons in the blazar jet and γ -rays from the interactions of the protons are present but not dominant.

With respect to the time-dependent radiation modelling of e.g. Petropoulou et al. (2016) our semi-analytic approach has the advantage of fast computation with reasonable accuracy, which allows for parameter-space scans and application to multiple sources. We have benchmarked our method against the time-dependent radiation modelling of Keivani et al. (2018) and find agreement within a factor of two for the expected neutrino flux between the two approaches.

In Section 2 we present the flare sample used in this work. In Section 3 we present the adopted neutrino modelling formalism, the blazar SED fitting method and the neutrino flux calculation procedure. Section 4 presents our results. We discuss the implications of our findings and conclude in Section 5. We assume a flat Universe with $\Omega_M = 0.3$, $\Omega_\Lambda = 0.7$ and $H_0 = 70 \text{ km s}^{-1} \text{ Mpc}^{-1}$.

2 DATA SELECTION

To calculate the expected neutrino output from individual blazar flares, an essential ingredient is the availability of multi-wavelength, and simultaneous observations of the broadband SED of the blazar. If hadrons exist in sufficient amounts, neutrinos are produced by the interactions of the hadrons with photons in the jet and external fields, when the latter are present.

Since its launch in June 2008, *Fermi*-LAT surveys the entire sky every three hours, allowing for the first time monitoring of a sizeable number of blazars in the 30 MeV- 300

GeV energy band (Fermi-LAT Collaboration 2009). Unfortunately, a similar monitoring instrument does not exist in other wavelengths at present. Several optical programs perform follow-up observations of *Fermi* monitored blazars (Bonning et al. 2012; Smith et al. 2009), and there are similar programs in the radio band (Richards et al. 2011; Jorstad & Marscher 2016). The *Swift*, *Integral*, and since more recently *NuSTAR* (Harrison et al. 2013) telescopes perform ToO observations to better cover the multi-wavelength SEDs, generally after being triggered due to extraordinary activity at a different wavelength. Very-high-energy (VHE) γ -ray telescopes also perform monitoring and follow-up observations of sources seen in exceptionally high-states by *Fermi* or other instruments.

Since a complete sample of flares does not exist, except in the *Fermi* energy band, our ability to model the neutrino emission from individual blazar flares is constrained by the availability of simultaneous data. For this work, we collected publicly available data for recorded flaring episodes of 12 *Fermi* bright BL Lacs, for which simultaneous (or semi-simultaneous) observations exist, with sufficient spectral coverage as to infer the main characteristics of the SED with reasonable confidence (for example the peak synchrotron frequency and peak synchrotron flux). Neutrino production is expected to be much more efficient in FSRQs than in BL Lac objects due to the higher-powers and existence of external photon fields (Atoyan & Dermer 2003). However, these also introduce additional free parameters. Therefore in this work we have considered only objects classified as BL Lacs.

We use simultaneous or quasi-simultaneous observations of the sources at all wavelengths since we want to calculate the neutrino output during the flaring state. All the blazars we have studied are monitored in the optical (R-band) by the Tuorla long-term monitoring program (Nilsson et al. 2018). Additionally, most are monitored by the Stewart Observatory *Fermi* blazar monitoring program (Smith et al. 2009), and several are monitored in the optical and near-infrared by SMARTS (Bonning et al. 2012). The details of all the flares in our sample are given in Table 1. Below we briefly present them in chronological order.

2.1 3C 66A

The blazar 3C 66A is classified as an ISP. It has recently been possible to determine the redshift of 3C 66A by association with its host galaxy cluster as $z = 0.34$ (Torres-Zafra et al. 2018). We use this latter value for neutrino calculations. In October 2008 3C 66A underwent a strong flare which triggered *Fermi*, and subsequently a multi-wavelength campaign, which we model in this work.

2.2 AO 0235+164

AO 0235+164 was monitored by a multi-wavelength campaign between 2008 - February 2009. AO 0235+164 is generally classified as a BL Lac, though based on the equivalent width of its H α line it would be classified as an FSRQ (D’Elia et al. 2015). During the 2008-9 campaign AO 0235+164 underwent a series of high states, most prominently between MJD 54750-54570. During this time its SED

exhibited a hard X-ray feature, consistent with arising from bulk Compton emission from cold electrons confined in the jet (Fermi-LAT Collaboration, et al. 2012). We conservatively model the neutrino emission during the 2008 flare of AO 0235+164 without considering this bulk Compton component or additional external photon fields only expected in FSRQs. AO 0235+164 experienced a second, approximately year-long, phase of flaring starting in August 2015 in the *Fermi* band (Ciprini 2015; Carrasco et al. 2015). Though a simultaneous SED with sufficient multi-wavelength coverage could not be obtained for the 2015 flare we comment on the likely neutrino production during this flare in Section 4.

2.3 Mrk 421

Mrk 421 is an HSP BL Lac, and one of the best-studied blazars, due to its proximity at $z = 0.031$. In March 2010, it underwent a ~ 13 -day flare, which triggered a very extensive multi-wavelength observation campaign (MAGIC Collaboration, et al. 2015b). This flare was extensively studied numerically in Petropoulou et al. (2016) in the context of lepton-hadronic neutrino production. We include it in our sample to facilitate a comparison between this well-studied source and other sources.

2.4 PG 1553+113

PG 1553+113 is an HSP BL Lac with uncertain redshift. With declination $+11.19^\circ$ it lies in a part of the sky that IceCube is most sensitive to, and has been considered as a candidate source of astrophysical neutrinos in several earlier studies (Neronov & Ribordy 2009; Cerruti et al. 2017; Petropoulou et al. 2015). In April 2012 it underwent a major flare in the VHE γ -ray band and was the subject of a large multi-wavelength campaign between February-August of the same year (MAGIC Collaboration et al. 2015a). Constraints on the redshift of PG 1553+113 come from the detection of Ly α absorption in its optical spectrum (Danforth et al. 2010), and the imprint of the EBL on its VHE spectrum. Here we assume $z = 0.4$, which was deemed the most likely value in MAGIC Collaboration et al. (2015a).

2.5 1ES 1959+650

1ES 1959+650 is a nearby, $z = 0.047$ HSP BL Lac. In June 2002 it underwent an orphan TeV flare (VERITAS Collaboration 2003; Krawczynski et al. 2004; VERITAS Collaboration 2005), not compatible with a one-zone SSC interpretation (e.g. Böttcher 2005). A search for neutrinos in the AMANDA data revealed three neutrinos coincident with the flaring activity (Ackermann et al. 2005). We model the 2012 flare of this source reported in VERITAS Collaboration, et al. (2014). A VHE flare was seen on MJD 56067, though no strong flare was seen in the *Fermi* data. We refer to this as flare 1ES 1959+650a. We also make predictions for the October 2015 outburst (Kaur et al. 2017), which we refer to as 1ES 1959+650b. The source underwent strong flaring in the γ -ray band in 2016 (see IceCube Collaboration 2017b and references therein), but the SED for this time is not yet publicly available. A limit to the neutrino output of this flare was presented in IceCube Collaboration (2017b).

Table 1. The list of flares studied in this work. For each flare the table lists the redshift (or assumed redshift) of the source, declination, and a reference time that roughly corresponds to the onset of the flare in MJD-i.e. Modified Julian Date, t_{ref} . In addition, the month of onset of the flare, references where the flare campaigns were presented, IceCube configuration at the time of the flare, the blazar classification of each source, and selection band for each flare are listed. For IceCube partial configuration definitions see Table B1.

Source	z	decl.	t_{ref} [MJD]	UT	Data Ref.	Config.	Type	Selection Band
3C 66A	0.34	+43.04	54747	Oct 2008	1	IC40	ISP	VERITAS
AO 0235+164	0.94	+16.62	54761	Oct 2008	2	IC40	LSP	<i>Fermi</i>
Mrk 421	0.031	+38.21	55265	Mar 2010	3	IC59	HSP	MAGIC
PG 1553+113	~ 0.4	+11.19	56037	Apr 2012	4,5	IC86	HSP	MAGIC
1ES 1959+650a	0.048	+20.00	56066.5	May 2012	6	IC86	HSP	VERITAS
Mrk 501	0.033	+39.76	56087	Jun 2012	7	IC86	HSP	MAGIC
S5 0716+714	< 0.32	+71.37	57045.5	Jan 2015	8,9	IC86	ISP/LSP	Optical/NIR
S4 0954+65	≥ 0.45	+65.57	57050	Feb 2015	10,11	IC86	HSP	<i>Fermi</i>
BL Lac	0.07	+42.28	57192	Jun 2015	12	IC86	ISP	<i>Fermi</i>
S2 0109+22	0.36	+22.74	57228	Jul 2015	13	IC86	ISP	<i>Fermi</i>
1ES 1959+650b	0.048	+20.00	57285	Sep 2015	14	IC86	HSP	<i>Fermi</i>
OJ 287	0.306	+20.11	57359	Dec 2015	15	IC86	LSP	theoretical
TXS 0506+056	0.3365	+5.70	58002	Sep 2017	16	IC86	ISP	<i>Fermi</i>

References: 1 - [Fermi-LAT Collaboration, et al. \(2011\)](#). 2 - [Fermi-LAT Collaboration, et al. \(2012\)](#). 3 - [MAGIC Collaboration, et al. \(2015b\)](#). 4,5 - [H.E.S.S. Collaboration \(2015\)](#); [MAGIC Collaboration et al. \(2015a\)](#). 6 - [VERITAS Collaboration, et al. \(2014\)](#). 7 - [MAGIC Collaboration, et al. \(2018d\)](#). 8 - [Chandra et al. \(2015\)](#), 9-[Manganaro et al. \(2016\)](#). 10, 11 - [Tanaka et al. \(2016\)](#); [MAGIC Collaboration et al. \(2018b\)](#). 12 - [MAGIC Collaboration et al. \(2019\)](#). 13 - [MAGIC Collaboration et al. \(2018a\)](#). 14 - [Kaur et al. \(2017\)](#). 15 - [Kushwaha et al. \(2018a\)](#). 16 - [IceCube Collaboration et al. \(2018\)](#).

2.6 Mrk 501

Mrk501, the second nearest BL Lac, at $z = 0.034$ is also an HSP. A number of multi-wavelength campaigns have been coordinated to monitor Mrk501 in the last ten years ([MAGIC Collaboration, et al. 2017, 2018d](#); [H.E.S.S. Collaboration 2019](#)). The largest observed VHE flare of this source since 1997 was analysed in [MAGIC Collaboration, et al. \(2018d\)](#) during a time when Mrk 501 was in an extreme HSP phase and is the focus of our study of this source. The VHE flare lasted one day (MJD 56087), while the *Swift* flare lasted until MJD 56089. The duration of this flare in the *Fermi* energy range is ~ 1 week.

2.7 S5 0716+714

The BL Lac S5 0716+714 exhibited an unprecedented optical/NIR flare on January 2015, which triggered multi-wavelength observations, and detection up to VHE energies with MAGIC ([Chandra et al. 2015](#); [MAGIC Collaboration, et al. 2018c](#); [Manganaro et al. 2016](#)). It is classified as an ISP ([Giommi et al. 1999](#)). Its redshift has not been directly measured due to a featureless optical spectrum ([Paiano et al. 2017](#)), but detection of Ly α absorption at the UV part of its spectrum puts it at $z < 0.32$ with 95% confidence ([Danforth et al. 2013](#)), consistent with the estimate of [Nilsson et al. \(2008\)](#) based on marginal detection of the host galaxy.

2.8 S4 0954+65

During February 2015, the *Fermi* flux of S4 0954+65 increased by a factor of ~ 40 (see Figure A1). The classification of this source has been debated, but the latest high-signal-to-noise spectroscopic observations classify it as a BL Lac with unknown redshift ([Landoni et al. 2015](#)). Even if S4 0954+65 is an FSRQ, as has been claimed previously, our SSC model results here are valid as a minimal neutrino scenario for this

source at its assumed redshift. In the absence of a firm measurement of the redshift of S4 0954+65, we assume the lower limit of [Landoni et al. \(2015\)](#), who obtained $z \geq 0.45$. In this sense, our estimate of the neutrino flux from the February 2015 flare of S4 0954+65 is optimistic.

2.9 BL Lac

BL Lacertae, at the redshift of $z = 0.069$, is the prototype of the BL Lac blazar type. The source flares very regularly in the *Fermi* band. Here we model the June 2015 flare of BL Lac, which triggered a multi-wavelength campaign ([Tsuji-moto et al. 2017](#); [MAGIC Collaboration et al. 2019](#)).

2.10 S2 0109+22

The ISP S2 0109+22 was observed to be in a high state in July 2015 by the *Fermi*-LAT. Multi-wavelength observations revealed a VHE flare on July 24th (MJD 57228). The most likely redshift of S2 0109+22 has been determined to be $z = 0.36$, based on association with its host cluster ([MAGIC Collaboration et al. 2018a](#)).

2.11 OJ 287

OJ 287 is a blazar known to exhibit a 12-year periodicity of its optical brightness ([Shi et al. 2007](#)), thought to host a binary supermassive black hole ([Valtonen et al. 2006](#)). In December 2015, it underwent the latest of a series of quasi-periodic optical outbursts. High variability from near-infrared to *Fermi*-LAT energies was exhibited between November 2015-May 2016, specifically MJD 57315 - 57460 ([Kushwaha et al. 2018a](#); [Kushwaha et al. 2019](#)). It further underwent intense near-infrared and X-ray variability between September 2016-July 2017 and was at the time detected at > 100 GeV by VERITAS ([O'Brien 2017](#)). Here we model the December 2015 flare. We were unable to fit

the subsequent bursts of this source within our single-zone formalism.

2.12 TXS 0506+056

We include in our sample the 2017 flare of TXS 0506+056 to allow for comparison of relative neutrino signal expectations in different blazar flares. The neutrino signal from this flare, coincident with IceCube-170922A was modelled extensively (MAGIC Collaboration 2018; Cerruti et al. 2019; Gao et al. 2019; Keivani et al. 2018; Murase et al. 2018; Liu et al. 2019; Padovani et al. 2018; Oikonomou et al. 2019). We do not attempt to model the 2014-15 flare of TXS 0506+056 here, as it would not fulfill our selection criteria based on γ -ray/X-ray or optical flaring. The 2014-15 flare of TXS 0506+056 was studied in Murase et al. (2018); Reimer et al. (2018); Rodrigues et al. (2019); Wang et al. (2018). In Padovani et al. (2019) evidence was presented that TXS 0506+056 is, despite its generally accepted classification, intrinsically an FSRQ. In this sense, the SSC model for this source (Normalisation A) is conservative, but the comparison to other BL Lac objects under fixed model assumptions is instructive.

3 MODEL OF BLAZAR EMISSION

We assume that the synchrotron and synchrotron self-Compton (SSC) mechanisms produce the bulk of the emission in the studied sources, i.e. electrons produce synchrotron photons responsible for the low-energy bump of the SED, and then they Compton scatter them to high energies producing the high-energy hump. In the SSC model, the simultaneous determination of the peak synchrotron frequency, ν_S , the peak inverse-Compton frequency, ν_C , the luminosity of the synchrotron peak, L_S , and of the self-Compton peak L_C , allows us to uniquely determine the physical parameters of the system.

The Doppler factor, δ , characterises the relativistic effects of the observed radiation from the blazar, and is given by $\delta = [\Gamma(1 - \beta \cos \theta)]^{-1}$, where Γ is the bulk Lorentz factor, θ the angle of motion in the jet with respect to the observer's line of sight, and $\beta = v/c$. In this work, we will assume the special case where $\theta \sim 1/\Gamma$, which implies $\delta \sim \Gamma$ (see e.g. Appendix A and B of Urry & Padovani 1995). From this point on, we will use δ and Γ interchangeably. In the SSC formalism δ is given by (Ghisellini et al. 1996; Tavecchio et al. 1998),

$$\delta \simeq 6.5 \left(\frac{\nu_C}{c^{3/2} t_{\text{var,d}} \nu_S^2} \right)^{1/2} \left[\frac{L_{S,\text{bb}}^2}{L_{C,\text{bb}}} \right]^{1/4}, \quad (1)$$

where $t_{\text{var,d}}$ the variability timescale of the system in days. Here, $L_{S(C),\text{bb}}$ are the broad-band luminosities which relate to the peak luminosities as $L_{S(C),\text{bb}} = f(b) \cdot L_{S(C)}$, where $L_{S(C)} = 4\pi d_L^2 \nu_S F_\nu^{S(C)}$, with $\nu_S(C) F_\nu^{S(C)}$ the peak fluxes and, d_L the luminosity distance to the source. The factor $f(b) \simeq 3 - 5$, is a constant of integration dependent on the exact shape of each hump of the SED (see Section 3.3). Equation 1 is valid when the inverse Compton process proceeds in the

Thomson regime. The magnetic field strength is given by,

$$B \simeq 2.4 \times 10^{-11} \text{ G} \cdot (1 + z) \cdot \frac{\nu_S^{3/2} t_{\text{var,d}}^{1/2}}{\nu_C^{3/2}} \left[\frac{L_C / 10^{45} \text{ erg/s}}{(L_S / 10^{45} \text{ erg/s})^2} \right]^{1/4}. \quad (2)$$

When the self-Compton process is in the Klein-Nishina regime, the values of ν_C and L_C are affected. The condition for the Klein-Nishina regime to severely affect the luminosity at the peak Compton frequency can be expressed in terms of a limiting Doppler factor, δ_{KN} , above which revision of Equations 1 and 2, is necessary,

$$\delta_{\text{KN}} = \left[\frac{\nu_C \nu_S}{(3/4)(m_e c^2 / h)^2} \right]^{1/2}, \quad (3)$$

where m_e , h , and c are the electron mass, Planck constant, and speed of light in cgs units respectively. Equations 1, 2 and 3 above are valid when all quantities are in cgs units, except the variability timescale which is in days.

3.1 High-energy neutrino production in the relativistic blob

High-energy neutrinos are produced by the decay of charged pions from the interactions of relativistic protons with photons, and matter (gas). In blazar jets interactions of relativistic protons with the ambient matter should be subdominant as energetics arguments constrain gas densities to be rather low in steady jets (Atoyan & Dermer 2003). The protons interact with ambient photons in the jet, which, in the case of BL Lacs are likely the synchrotron photons produced by co-accelerated electrons. In FSRQs, several other radiation fields, external to the jet, could provide an efficient target for the protons, namely from the accretion disk, or jet/accretion disk photons reprocessed in the Broad Line Region, or photons from the dust torus (Murase et al. 2014; Dermer et al. 2014; Rodrigues et al. 2018).

The threshold energy $E_{p,\text{th}}$ for highly relativistic protons to produce a pion in interactions with photons with energy ε_γ in the laboratory frame is

$$E_{p,\text{th}} = \frac{2m_p m_\pi + m_\pi^2}{4\varepsilon_\gamma} \approx 7 \times 10^{16} \left[\frac{\varepsilon_\gamma}{1 \text{ eV}} \right]^{-1}, \quad (4)$$

where m_p , m_π are the the proton and pion mass respectively, and we have given the expression in the case of a head-on collision. On average, in a py collision, $\sim 20\%$ of the proton energy goes to the pion, which decays to four leptons, which share the energy of the pion almost equally. Thus the characteristic neutrino energy with respect to the energy of the parent proton is given by

$$E_\nu \approx \frac{1}{20} E_p. \quad (5)$$

For the ~ 10 TeV-10 PeV neutrinos observed by IceCube the parent protons will have had characteristic energies $E_p \sim 10^{14} - 10^{17}$ eV.

We convert the observed photon spectral energy flux per decade of frequency of the source, $\nu_\gamma F_{\nu_\gamma}$, to the cosmic rest-frame luminosity per decade of photon energy, $\varepsilon_\gamma L_{\varepsilon_\gamma}$, using

$$\nu_\gamma F_{\nu_\gamma}(\nu_\gamma) = \frac{\varepsilon_\gamma L_{\varepsilon_\gamma}}{4\pi d_L^2}, \quad (6)$$

where, ε_γ , is the energy of the photon in the cosmic rest frame, and d_L the luminosity distance. The comoving luminosity of the blob is calculated using $\Gamma^4 L'_{\varepsilon_\gamma} \varepsilon'_\gamma = \varepsilon_\gamma L_{\varepsilon_\gamma}$. Here, and in what follows we denote comoving frame quantities as primed, observer-frame quantities are unscripted, and quantities in the cosmic rest frame are scripted.

We assume that the neutrino production region is a relativistic blob in the blazar jet, spherical in the comoving frame. The comoving target photon density n'_{ε_γ} in the jet zone, where neutrino production is expected to be taking place is given by

$$n'_{\varepsilon_\gamma} = \frac{3L'_{\varepsilon_\gamma}}{4\pi r_b'^2 c \varepsilon'_\gamma}. \quad (7)$$

Here r'_b is the comoving radius of the neutrino emission region, which we infer from the (comoving) variability timescale t'_{var} . We calculate t'_{var} as $t'_{\text{var}} = \Gamma \cdot t_{\text{var}}/(1+z)$, with t_{var} the observed variability timescale, and r'_b ,

$$r'_b \sim c \cdot t'_{\text{var}}. \quad (8)$$

We use the shortest available variability timescale for each of the studied flares. If the true variability of the system is smaller than can be inferred from observations due to low statistics, and r'_b is smaller than in our calculations, our predicted neutrino fluxes in the SSC model are conservative, as the number density of target photons, and therefore the optical depth to photo-meson production is underestimated, as shown by Equation 7 (the situation is however different in the external-Compton model in our setup, where typically the external-Compton neutrino component is the dominant one. In the latter case, a larger r'_b implies a larger maximum proton energy and this affects the resulting neutrino spectrum).

The maximum proton energy for each flare is determined by comparing the acceleration timescale to the timescales of dominant cooling processes t_{cool} ,

$$t_{\text{acc}}^{-1} > t_{\text{cool}}^{-1} \equiv t_{\text{dyn}}^{-1} + t_{p,\text{syn}}^{-1} + t_{p\gamma}^{-1} + t_{\text{BH}}^{-1}, \quad (9)$$

where the synchrotron cooling time of species i is given by $t_{i,\text{syn}}^{-1} = 6\pi m_i^4 c^3 / (m_e^2 \sigma_T B^2 \varepsilon_i)$, and $t_{\text{dyn}}^{-1} = r'_b/c$ is the dynamical timescale of the system, which sets the timescale for adiabatic cooling of the emitting region.

Finally, $t_{\text{acc}}^{-1} = \eta \varepsilon'_p / (ceB')$, is the proton acceleration timescale, for protons assumed to undergo second order Fermi acceleration. The acceleration efficiency is parametrised by $\eta \geq 1$, with $\eta = 1$ corresponding to the fastest possible acceleration time, when diffusion proceeds in the Bohm limit. For a typical BL Lac emitting region in our model with $B' = 1$ G, $r'_b \sim 10^{17}$ cm, and $\Gamma = 10$, this leads to proton maximum energy, $\varepsilon'_p \approx 1$ EeV, when $\eta = 1$, subject to details of the photon density of the source.

We also consider a higher value of η , namely $\eta = 10^4$. A large value of η in the blazar emitting region was inferred by Inoue & Takahara (1996); Inoue & Tanaka (2016) and a natural interpretation of these results was given by Dermer et al. (2014) in the context of stochastic acceleration. Physically, a large value of η corresponds to a low level of turbulence or otherwise inefficient scattering of the cosmic rays in the acceleration zone, leading to inefficient acceleration. The case in which η is large is further motivated by

the results of leptonic models, where the maximum proton energy is shown to be $\lesssim 100$ PeV to provide a good fit to the source SED (Dimitrakoudis et al. 2014)², and by the observation that for the 2017 flare of TXS 0506+056 it is impossible to have UHECR acceleration and efficient sub-PeV neutrino production simultaneously. Namely, a maximum proton energy higher than $\varepsilon'_p \sim \text{EeV}$ would produce a neutrino spectrum that peaks beyond 50 PeV and the sub-PeV neutrino flux would be highly suppressed (Keivani et al. 2018; Gao et al. 2019).

The photomeson energy-loss timescale is estimated as,

$$t_{p\gamma}^{-1} = \frac{c}{2\gamma_p^2} \int_{\bar{\varepsilon}_{\text{th}}}^{\infty} d\bar{\varepsilon}'_\gamma \sigma_{p\gamma} \kappa_{p\gamma} \bar{\varepsilon}'_\gamma \int_{\bar{\varepsilon}'_\gamma/(2\gamma_p)}^{\infty} d\varepsilon'_t \varepsilon_t'^{-2} n'_{\varepsilon_t}. \quad (10)$$

Here, $\bar{\varepsilon}_{\text{th}} \sim 145$ MeV is the threshold energy for pion production in the rest frame of the proton, and $\sigma_{p\gamma}$ and $\kappa_{p\gamma}$ are the cross-section and inelasticity of photon-meson interactions, respectively. We adopt the parametrisations used by Murase & Nagataki (2006) for $\sigma_{p\gamma}$ and $\kappa_{p\gamma}$. The quantity n'_{ε_t} is the target photon density given in Equation 7, differential in energy. We calculate the fraction of energy converted to pions, as $f_{p\gamma} \equiv t'_{\text{cool}}/t'_{p\gamma}$.

Our treatment does not include Bethe-Heitler photo-pair production. Due to the low value of the effective inelasticity $\kappa_{\text{BH}} \sim m_e/m_p$ in comparison to that of photo-pion interactions with $\kappa_{p\gamma} \gtrsim 0.2$, the relative energy-loss rate for protons interacting with photons at the peak of the νF_ν spectrum is,

$$\frac{\kappa_{p\gamma} \sigma_{p\gamma}}{\kappa_{\text{BH}} \sigma_{\text{BH}}} \sim 100, \quad (11)$$

where σ_{BH} is the Bethe-Heitler photo-pair cross-section. The relative importance between Bethe-Heitler and photo-pion interactions depend on photon spectra Murase et al. (2018). The Bethe-Heitler photo-pair production is subdominant as a proton cooling process and can be neglected when the target photon spectrum is sufficiently hard (see e.g. Fig. 2 of Petropoulou & Mastichiadis 2015 and Equation 10 of Murase et al. 2018). On the other hand, it can produce a radiative signature on the blazar SED, for example, when the proton content of the jet becomes extremely large as shown in Petropoulou & Mastichiadis (2015); Keivani et al. (2018). We do consider this effect in later sections.

We assume a power-law proton spectrum, $dN'_p/d\varepsilon'_p \propto \varepsilon_p'^{-2}$, with an exponential cut-off beyond the maximum attainable proton energy, determined by comparing the acceleration timescale to the cooling time at each proton energy. We consider the existence of protons with Lorentz factor as low as $\gamma_{p,\text{min}} = 1$.

We normalise the total proton luminosity of the source, \mathcal{L}'_p , to the total (isotropic equivalent) comoving photon luminosity \mathcal{L}'_γ , assuming $\mathcal{L}'_p = \xi_{\text{cr}} \mathcal{L}'_\gamma$, with ξ_{cr} the baryon loading factor.

We consider two possible scenarios for the physical parameters in the sources, detailed below:

- **Normalisation A (UHECR / conservative):** Here, the baryon loading is relatively low, $\xi_{\text{cr}} = 10$, and the maximum proton energy is high (the acceleration efficiency is

² Referred to as *leptohadronic* therein.

high, with $\eta = 1$). This roughly corresponds to the average baryon loading needed for blazars to power the locally observed UHECR production rate of $E_{\text{UHE}} Q_{E_{\text{UHE}}} \sim 10^{44} \text{ erg s}^{-1} \text{ yr}^{-1}$ at $\gtrsim 5 \times 10^{18} \text{ eV}$ (Waxman 1995; Berezhinsky et al. 2006; Murase & Takami 2009; Katz et al. 2013; Pierre Auger Collaboration 2017), as calculated in Murase et al. (2014). The neutrino spectra obtained with this model typically peak beyond 10 PeV, which is typical in canonical blazar neutrino models. In general, in models that link the neutrino flux to the UHECR flux it is typically expected that $\xi_{\text{cr}} \lesssim 100$, sensitive to the power-law index of the injected proton spectrum (Murase et al. 2014).

• **Normalisation B (TXS 0506+056 / optimistic):**

This is inspired by the most optimistic model of Keivani et al. (2018), LMPL2b, for the September 2017 flare of TXS 0506+056 (see also their Table 7) if IceCube-170922A was indeed produced by TXS 0506+056. Assuming this model, Keivani et al. (2018) estimated the number of neutrinos expected from TXS 0506+056 during the ~ 180 -day flare in 2017, below 10 PeV, $N_{\nu_{\mu} < 10 \text{ PeV}}/180 \text{ days} = 10^{-2}$ in the EHE alert channel. The baryon loading factor is high, $\xi_{\text{cr}} = 1540$. The maximum proton energy is low, with $\eta = 10^4$, and as a result the neutrino spectrum typically peaks at lower, \sim sub-PeV, energies than with Normalisation A.

In general, the baryon loading of the jet cannot not exceed the value considered in Normalisation B as the interactions of the protons would produce not only neutrinos but also secondary γ -rays and electron-positron pairs from the interactions of the protons inside the source. These high-energy secondary leptons when produced in the interactions of protons further interact redistributing power from high to lower energies, typically in the keV and MeV energy range. Too large a proton content then means that these electromagnetic cascade products would exceed the simultaneous SED in the keV and MeV energy range, as shown in e.g. Petropoulou & Mastichiadis (2015); Murase et al. (2018); Reimer et al. (2018); Rodrigues et al. (2019).

For some sources in our sample, Normalisation B contradicts the SED, in the sense that such a high proton luminosity in the source would produce electromagnetic cascade emission from the electrons, positrons (and photons) produced by the Bethe-Heitler photopair (photopion) interaction of the protons, that would exceed the observed SED in the keV energy range in single-zone, standard emission scenarios. In what follows we have chosen to fix the baryon loading factor and maximum proton energy across all sources to facilitate an intuitive comparison between the sources. Where the cascade emission overshoots the SED within the model assumptions of Normalisation B, we lower the baryon loading to an appropriate level to not exceed the cascade bounds and note the different treatment in the results that follow.

A summary of the models considered, and relevant model parameters is given in Table 2. Figure 1 shows the relevant cooling timescales for the January 2015 flare of S5 0716+714 in the SSC only scenario (Normalisation A). The maximum proton energy, in this case, is set by the escape timescale, t'_{dyn} , and other cooling processes, including synchrotron cooling of protons are subdominant. This is typically the case in the blazar blob in the leptonic models investigated here. Using Normalisation B, the main differences

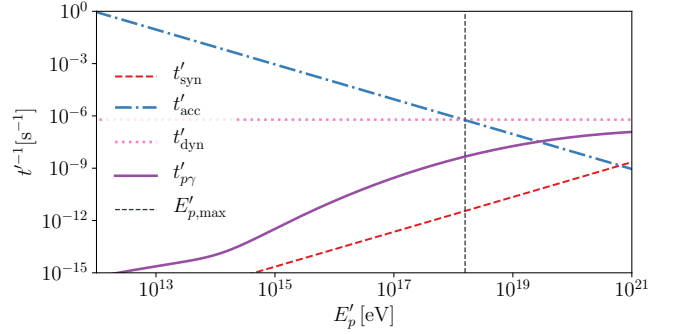


Figure 1. Cooling timescales relevant for neutrino production during the January 2015 flare of S5 0716+714 in the SSC only scenario (Normalisation A). The definition of the cooling timescales is given in Section 3.1.

Table 2. Table of parameters for the fiducial models tested in this work, namely the baryon loading factor ξ_{cr} , the efficiency of particle acceleration η , the minimum proton Lorentz factor, $\gamma_{p,\text{min}}$, and the energy density of the external radiation field in the comoving frame u'_{ext} .

Normalisation	A (UHECR)	B (LMPL2b)
ξ_{cr}	10	1540
η	1	10^4
$\gamma_{p,\text{min}}$	1	1
u'_{ext}	N/A	varies by source see Table 3

are that the $p\gamma$ interaction timescale, $t'_{p\gamma}$ is significantly enhanced, due to the presence of an additional target photon field and the maximum proton energy is low because the acceleration efficiency is lower and therefore t'_{acc} is much larger.

The muon neutrino spectrum produced by pion decay following $p\gamma$ interactions is calculated as,

$$\varepsilon_{\nu_{\mu}}^2 \frac{dN'_{\nu_{\mu}}}{d\varepsilon'_{\nu_{\mu}}} \approx \frac{1}{8} \cdot f'_{p\gamma} \cdot f'_{\pi,\text{cool}} \cdot \varepsilon_p'^2 \frac{dN'_p}{d\varepsilon'_p}, \quad (12)$$

for the muon neutrinos produced by the decay of the pion, and,

$$\varepsilon_{\nu_{\mu}}^2 \frac{dN'_{\nu_{\mu}}}{d\varepsilon'_{\nu_{\mu}}} \approx \frac{1}{8} \cdot f'_{p\gamma} \cdot f'_{\pi,\text{cool}} \cdot f'_{\mu,\text{cool}} \cdot \varepsilon_p'^2 \frac{dN'_p}{d\varepsilon'_p}, \quad (13)$$

and

$$\varepsilon_{\nu_e}^2 \frac{dN'_{\nu_e}}{d\varepsilon'_{\nu_e}} \approx \frac{1}{8} \cdot f'_{p\gamma} \cdot f'_{\pi,\text{cool}} \cdot f'_{\mu,\text{cool}} \cdot \varepsilon_p'^2 \frac{dN'_p}{d\varepsilon'_p}, \quad (14)$$

for muon and electron neutrinos produced by the subsequent decay of the muon respectively. In the above, $f_{\pi,\text{cool}} = 1 - \exp(-t_{\pi,\text{cool}}/t_{\pi,\text{dec}})$, and equivalently $f_{\mu,\text{cool}}$, are suppression factors due to the cooling of pions and muons respectively. The decay time of the pions is, $t_{\pi,\text{dec}} \approx \gamma_{\pi} \tau_{\pi}$, with $\gamma_{\pi} = \varepsilon_{\pi}/(m_{\pi} c^2)$, and $\tau_{\pi} = 2.6 \times 10^{-8} \text{ s}$ the mean rest frame lifetime of the pions. The cooling time for pions is obtained from $t_{\pi,\text{cool}}^{-1} = t_{\pi,\text{syn}}^{-1} + t_{\pi,\text{dyn}}^{-1}$. In the same way we obtain the cooling of the muons, with $\tau_{\mu} \approx 2.2 \times 10^{-6} \text{ s}$.

Neutrino oscillation over large distances modifies the

initial flavour distribution of neutrino fluxes. The measurable muon neutrino flux on Earth is given by,

$$\varepsilon_{\nu_\mu, \text{Earth}}'^2 \frac{dN'_{\nu_\mu, \text{Earth}}}{d\varepsilon'_{\nu_\mu, \text{Earth}}} = P_{\nu_\mu \rightarrow \nu_\mu} \cdot \varepsilon_{\nu_\mu}'^2 \frac{dN'_{\nu_\mu}}{d\varepsilon'_{\nu_\mu}} + P_{\nu_e \rightarrow \nu_\mu} \cdot \varepsilon_{\nu_e}'^2 \frac{dN'_{\nu_e}}{d\varepsilon'_{\nu_e}}, \quad (15)$$

where $P_{\nu_i \rightarrow \nu_j}$ are mixing probabilities, and $P_{\nu_i \rightarrow \nu_i}$ unitarity relations, the relevant ones for our calculation being $P_{\nu_e \rightarrow \nu_\mu} \approx 0.24$, $P_{\nu_\mu \rightarrow \nu_\mu} \approx 0.37$ (Pakvasa et al. 2008).

As explained in Section 3.4, we consider only “up-going” muon neutrinos, that is muon neutrinos from the Northern sky entering the detector from below, in this work, primarily due to the higher exposure than e.g. HESE events.

3.2 Neutrino production in interactions with external fields

From the point of view of neutrino production, the SSC model is conservative in the sense that the hadrons in the source can only interact with co-accelerated photons in the relativistic blob. In the comoving frame this radiation field is not boosted, and therefore the energy density, u'_{syn} , relevant for neutrino production, is relatively low. In addition to neutrino production in the relativistic blob, we study an optimistic scenario for the production of neutrinos, by considering the existence of external photon fields.

In BL Lac objects, the broad-line region is either non-existent or too weak to be observed. But some of the sources we studied, even though classified as BL Lacs are likely FS-RQs in reality, and thus possess a strong broad-line region. In fact, for several of the sources in our sample, the broad-line region luminosity has been measured (e.g. Sbarrato et al. 2012, 2014; Padovani et al. 2019). On the other hand, even when a powerful broad line region does exist, it is not guaranteed that it will contribute to neutrino production because the emitting region of the jet may be at larger jet radii. This is for example, on average, the case in the study of Costamante et al. (2018).

Though true BL Lac objects are not observed to possess a broad-line region, the existence of a spine-layer, or spine-sheath model, has been proposed as an explanation for the observation of strongly superluminal motion in the TeV γ -ray emitting region, and slower motion on parsec scales measured with radio observations (Ghisellini et al. 2005). The sheath can also act as an efficient target for protons to interact with and produce neutrinos (Tavecchio et al. 2014; Tavecchio & Ghisellini 2015; MAGIC Collaboration 2018). Additionally, BL Lac objects possess radiatively inefficient accretion disks, thought to produce a complex, relatively broadband photon spectrum which can also act as a target field for neutrino production (Righi et al. 2019).

We consider a generic external photon field, inspired by the spine-sheath model, with a power-law spectrum, $n'_{\varepsilon'_i} \propto \varepsilon'^{-\alpha}_{i'}$, extending from $\varepsilon'_{i' \min} = 50$ eV to $\varepsilon'_{i' \max} = 5000$ eV in energy, and $\alpha = 2$ as in the LMPL2b model of Keivani et al. (2018). Though the exact shape of the emerging neutrino spectrum depends on the details of the target photon spectrum, the total neutrino production is proportional to the integral of the energy density of the external field. In this sense, the scenario we explore here is analogous to a physical set-up where the external target field

is a portion of the broad-line region as may be the case for TXS 0506+056 (Padovani et al. 2019).

We only consider scenarios where the SSC mechanism is the dominant mechanism responsible for the observed SED, in other words, $u'_{\text{syn}} > u'_{\text{ext}}$. The luminosity of the external field in the observer frame is calculated as,

$$L_{\text{ext}} = 4\pi R_{\text{ext}}^2 c u'_{\text{ext}} / \Gamma^2, \quad (16)$$

with R_{ext} the size of the system in its proper frame. For definiteness we fix $R_{\text{ext}} = 3 \times 10^{19}$ cm, which would encompass the large scale jet, noting that the setup is equivalent to one where the external radiation field is denser, but traversed over a shorter scale, as is the case if the emitting region is situated inside the broad-line region from the point of view of neutrino production and associated cascade/opacity constraints. As a starting estimate we use $u'_{\text{ext}} = u'_{\text{syn}}/2$. For all SEDs, we ensure, that L_{ext} is lower than the superluminal blob emission at all energies, if necessary by lowering u'_{ext} with respect to the starting estimate. The final values of u'_{ext} are given in Table 3. For AO 0235+164, S2 0109+22 and OJ 287 the opacity for 1 TeV γ -rays is greater than one. This is consistent with the SEDs of these sources whose γ -ray spectra show a cutoff at lower energies. An additional constraint on the energy density of any external radiation field in BL Lac objects comes from the relative strength and peak frequency of the two bumps of the SED (Tavecchio et al. 2019). In the case of HSP objects the upper limit on u'_{ext} is particularly tight, and often stronger than the constraint imposed by requiring transparency to TeV photons. We have checked that our assumed u'_{ext} is consistent with this additional requirement.

The presence of the stationary or quasi-stationary, meaning slow-moving, external field enhances the neutrino production efficiency, but at the same time the external photon field provides a target for $\gamma\gamma$ interactions, enhancing the opacity of the source to γ -rays. The optical depth for γ -rays with energy, ε_γ , via the $\gamma + \gamma \rightarrow e^+ + e^-$ process, in interactions with the external photon field, is given approximately by,

$$\tau_{\gamma\gamma}(\varepsilon_\gamma) \simeq \eta_{\gamma\gamma}(\alpha) \sigma_T (R_{\text{ext}}/\Gamma) u'_{\varepsilon'_i, \text{ext}} |_{\varepsilon'_i = m_e^2 c^4 / \varepsilon'_\gamma} \quad (17)$$

(see e.g. Rees 1967; Rees & Meszaros 1992; Murase et al. 2016). Here, $\eta_{\gamma\gamma}(\alpha)$ is an integration constant. For a power-law spectrum with $1 < \alpha < 7$ to a very good approximation $\eta_{\gamma\gamma}(\alpha) \approx 7/[6\alpha^{5/3}(1+\alpha)]$ (Baring 2006). We check that the opacity to γ -rays in our assumed external field is not too high, and therefore consistent with the γ -ray observations of all the flare SEDs. The optical depth for γ -rays with energy 100 GeV, and 1 TeV is also given in Table 3.

3.3 Blazar SED fitting method

We fit the blazar spectral energy distributions with two log-parabolic functions of the form

$$\nu_\gamma F_{\nu_\gamma} = \nu_{\gamma, \text{pk}} F_{\nu_{\gamma, \text{pk}}} \cdot 10^{b \cdot (\log(\nu_\gamma / \nu_{\gamma, \text{pk}}))^2}, \quad (18)$$

where b is the shape parameter and $\nu_{\gamma, \text{pk}}$ is the peak frequency of the log-parabola. It was shown in Massaro et al.

Table 3. The energy density of the external radiation field in the comoving frame u'_{ext} and the photon field comoving with the blob u'_{syn} , both in units of erg cm^{-3} , and optical depth for γ -rays with energy 100 GeV, and 1 TeV.

	u'_{syn}	u'_{ext}	$\tau_{\gamma\gamma}$ (100 GeV)	$\tau_{\gamma\gamma}$ (1 TeV)
3C 66A	10^{-4}	$5 \cdot 10^{-5}$	< 0.1	< 0.1
AO 0235+164	$6 \cdot 10^{-3}$	$3 \cdot 10^{-3}$	0.3	3.0
Mrk 421	$2 \cdot 10^{-4}$	$9 \cdot 10^{-5}$	< 0.1	0.1
PG 1553+113	$6 \cdot 10^{-4}$	$3 \cdot 10^{-3}$	< 0.1	0.1
1ES 1959+650a	$5 \cdot 10^{-5}$	$2 \cdot 10^{-5}$	< 0.1	< 0.1
Mrk 501	10^{-3}	$3 \cdot 10^{-4}$	< 0.1	0.5
S5 0716+714	$3 \cdot 10^{-3}$	$2 \cdot 10^{-3}$	0.1	0.8
S4 0954+65	$2 \cdot 10^{-3}$	$9 \cdot 10^{-4}$	< 0.1	0.3
BL Lac	$2 \cdot 10^{-2}$	$4 \cdot 10^{-4}$	< 0.1	0.1
S2 0109+22	$5 \cdot 10^{-3}$	$5 \cdot 10^{-3}$	0.2	1.7
1ES 1959+650b	$3 \cdot 10^{-5}$	10^{-5}	< 0.1	< 0.1
OJ 287	$6 \cdot 10^{-3}$	$2 \cdot 10^{-3}$	0.4	3.6
TXS 0506+056	$7 \cdot 10^{-4}$	$7 \cdot 10^{-4}$	< 0.1	0.2

(2004) that such a log-parabolic function is one of the simplest ways to represent curved spectra, while fitting the blazar spectral energy distributions in different luminosity states very well, and providing good estimates of the energy and flux of the SED. The observed log-parabolic shape of the SED can be explained as deriving from stochastic acceleration processes (Massaro et al. 2004; Tramacere et al. 2007; Stawarz & Petrosian 2008; Dermer et al. 2014) which produce a curved lepton spectrum from injection.

We perform two independent fits for the two humps of the SED. For the second hump of the SED we determine the best fit parameters of the expression $\nu_{\gamma} F_{\nu_{\gamma}} \cdot \exp(-\tau_{\gamma\gamma}(\varepsilon, z))$, where $\tau_{\gamma\gamma}(\varepsilon, z)$ is the optical depth of the extragalactic background light for photons of energy ε originating at a source at redshift z . We use the $\tau_{\gamma\gamma}(\varepsilon, z)$ calculated by Franceschini et al. (2008). We perform a numerical χ^2 minimisation (James 1994) to determine the parameters b and $\nu_{\gamma, \text{pk}}$ that provide the best fit for each SED.

The broad-band flux can be obtained by analytically integrating Equation 18 over the entire frequency range, which gives (Massaro et al. 2004),

$$F_{\text{bb}} = \sqrt{\pi \ln 10} \frac{\nu_{\gamma, \text{pk}} F_{\nu_{\gamma, \text{pk}}}}{\sqrt{b}}. \quad (19)$$

The simple log-parabola model does not fit the data well for energy distributions that do not decrease symmetrically with respect to the peak frequency. In this case, we fit the SEDs with a log-parabola with an exponential cutoff of the form

$$\nu_{\gamma} F_{\nu_{\gamma}} = \nu_{\gamma, \text{pk}} F_{\nu_{\gamma, \text{pk}}} \cdot 10^{\beta \cdot (\log(\nu_{\gamma}/\nu_{\gamma, \text{pk}}))^2} \cdot e^{-\nu_{\gamma}/\nu_{\gamma, \text{cut}}}. \quad (20)$$

We allow the optimal value of ν_{cut} , the extra-free parameter, to be determined independently for the two peaks through the minimisation procedure described above. The cutoffs in the two peaks need not necessarily have the same origin, even in the SSC model, which justifies our choice to fit them separately. The required cutoff in the synchrotron peak is likely due to cooling of the electrons, particularly for the conditions likely in HSPs, where the synchrotron emission extends to higher energies. On the other hand, a cutoff in the inverse Compton peak could be due to internal absorption in

Table 4. Table of the parameters for each of the flares studied in this work. The Doppler factor, δ , and magnetic field strength B in Gauss are taken from the literature, as stated in the references column. In addition, it is indicated whether the parameters were derived assuming only synchrotron-self Compton (SSC) emission or additional external-Compton emission (EC).

Source	δ	B	Model	Ref.
3C 66A	40	0.02	SSC	1
AO 0235+164	20	0.22	SSC+EC	2
Mrk 421	21	0.04	SSC	3
PG 1553+113	40	0.045	SSC	4
1ES 1959+650a	25	0.01	SSC	5
Mrk 501	10	0.02	SSC	6
S5 0716+714	25	0.10	SSC	7
S4 0954+65	30	0.6	SSC+EC	8,9
BL Lac	25	0.14	SSC+EC	10
S2 0109+22	22	0.05	SSC	11
1ES 1959+650b	25	0.01	SSC	5
OJ 287a	14	0.9	SSC+EC	12
TXS 0506+056	24	0.4	SSC+EC	13

References: 1 - Fermi-LAT Collaboration, et al. (2011).

2 - Fermi-LAT Collaboration, et al. (2012). 3 - MAGIC Collaboration, et al. (2015b). 4 - MAGIC Collaboration et al. (2015a). 5 - VERITAS Collaboration, et al. (2014). 6 - MAGIC Collaboration, et al. (2018d). 7 - Manganaro et al. (2016). 8,9 - Tanaka et al. (2016); MAGIC Collaboration et al. (2018b). 10 - MAGIC Collaboration et al. (2019). 11 - MAGIC Collaboration et al. (2018a). 12 - Kushwaha et al. (2018b). 13 - Keivani et al. (2018).

the various photon fields in the source. This can occur inside the emitting region, but also by interactions with external photon fields.

We can calculate the Doppler factor, δ , and the magnetic-field strength, B , using Equations 1 and 2, and the broad-band luminosity for each hump of the SED as given by Equation 19. However, when the cutoff is very close to the peak we cannot accurately determine δ and B from the SED with this method. This is the case for most of the HSP blazars in our sample. We have therefore opted to use literature values for δ and B , obtained from the modelling of the specific flares we study, throughout most of this work. The assumed Doppler factor δ , and magnetic field strength for each of the studied sources are given in Table 4. In Section 4.1, where we discuss the effect of systematic uncertainties on δ and B on neutrino flux expectations, we also compare the Doppler factors obtained with our log-parabolic model using Equations 1 and 2 with those from Table 4.

We also state in Table 4 whether a simple SSC model can fit the SED of each of the studied flares. In the cases where an external Compton component is required to fit the SED (denoted SSC+EC) our Normalisation A is conservative as interactions with additional external photon fields in the source environment are disregarded.

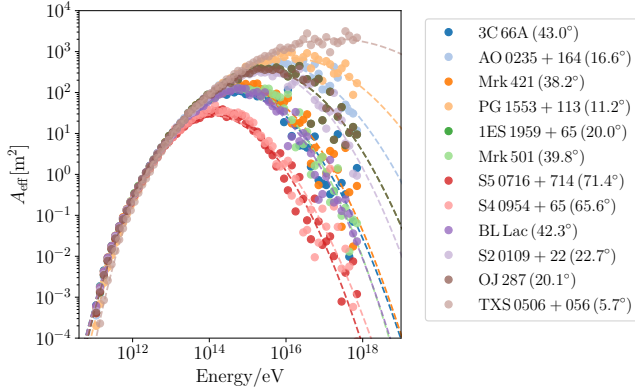


Figure 2. Effective area as a function of energy in IceCube IC86 configuration at the declination of each of the sources in our study. The filled circles show the IceCube Monte Carlo points from [IceCube Collaboration \(2019\)](#), and the dashed lines the parametrization used in this work.

3.4 Expected neutrino event counts

In this section, we outline the method we use to calculate neutrino counts in IceCube and future neutrino telescopes for a given source neutrino spectrum. We consider here only through-going muon neutrinos from the Northern sky. The better arrival direction reconstruction, higher statistics, and lower energy threshold make them more suitable for the search for faint signals from individual blazar flares than other event selections. Approximately 100000 neutrinos from the Northern sky are detected by IceCube each year ([IceCube Collaboration 2019](#)). Most of them are atmospheric neutrinos that form an irreducible background. However, the atmospheric neutrino spectrum is softer than the spectrum expected by astrophysical sources, including blazars. Hence, by constraining neutrino point-source searches to the highest-energies and the time-bin to the time of interest (in our case the blazar flare duration), the background rate is reduced significantly.

The instantaneous number of signal-only, *through-going* muon-neutrino events, $dN_{\nu, t_0}/dt$, expected to be detected by IceCube during a small time-interval dt during a neutrino flare is,

$$\frac{dN_{\nu, t_0}}{dt} = \int_{E_{\nu, \min}}^{E_{\nu, \max}} dE_{\nu} \frac{1}{3} A_{\text{eff}}(E_{\nu}, \theta) F_{E_{\nu}}, \quad (21)$$

where $E_{\nu, \min}$ and $E_{\nu, \max}$ are the minimum and maximum energy considered respectively, and $F_{E_{\nu}}$, the all-flavour neutrino flux, differential in energy.

The effective area of the neutrino detector for a neutrino arriving with zenith angle θ and energy E_{ν} is $A_{\text{eff}}(E_{\nu}, \theta)$. We use the full, zenith- and energy- dependent simulated effective area of the IceCube point-source analysis, $A_{\text{eff}}(E_{\nu}, \theta)$, given in [IceCube Collaboration \(2019\)](#).³ For each period when the IceCube detector was in incomplete configuration we use the corresponding simulated $A_{\text{eff}}(E_{\nu}, \theta)$ for that period. For years beyond 2011, we assume the IceCube configuration of 2011,

Table 5. Time duration of each of the flares investigated, ΔT , in days, based on the analysis of the high-energy FAVA data as detailed in Appendix A, or, in the absence of significant flux enhancement in the FAVA data, the flare timescale determined in a different waveband as stated. The Table also gives the timescale of smallest detected time-variability in days, $t_{\text{var}}^{\text{obs}}$, which we use to determine the size of the emitting region and waveband at which it was detected.

Source	$t_{\text{var}}^{\text{obs}}$	Band	ΔT	Band
3C 66A	1	VERITAS	14	FAVA
AO 0235+164	3	<i>Fermi</i> and others	84	FAVA
Mrk 421	1	MAGIC	13	MAGIC
PG 1553+113	1	<i>Swift</i> / MAGIC	30	<i>Swift</i> (XRT)
1ES 1959+650a	1	VERITAS	46	Optical
Mrk 501	0.2	MAGIC	21	FAVA
S5 0716+714	1	MAGIC	14	FAVA
S4 0954+65	1	<i>Fermi</i> and others	28	FAVA
BL Lac	0.1	MAGIC	7	FAVA
S2 0109+22	1	<i>Fermi</i> and others	21	FAVA
1ES 1959+650b	1	<i>Fermi</i> and others	84	FAVA
OJ 287	1	near-IR/UV	7	FAVA
TXS 0506+056	1	<i>Fermi</i> and others	175	FAVA

IC86. We are interested in the effective area of IceCube out to, and beyond 10^{18} eV. For this reason, we fit the IceCube effective area beyond 10^{18} eV, which is not publicly available, with a log parabolic function.

The left panel of Figure 2 shows the effective area of IceCube-IC86 as a function of energy at the declination of each of the sources in our sample. Filled circles show the IceCube Monte Carlo points from [IceCube Collaboration \(2019\)](#), and the dashed lines the fitted function used in this work.

We estimate the total number of neutrinos expected during the flare by integrating over the time duration of each flare, ΔT , as defined in Table 5 (based on the analysis of the FAVA lightcurves shown in Figure A1 as described in Appendix A). The estimate of the expected number of neutrinos takes into account the IceCube exposure during each flare given the source's declination and time of occurrence. To integrate over the duration of the flare we use the instantaneous SED obtained at the specified time of multi-wavelength observations, typically averaged to the nearest day, and use the relation,

$$\frac{dN_{\nu, t}}{dt} = \frac{dN_{\nu, t_0}}{dt} \cdot \frac{A_{\text{eff}, t}}{A_{\text{eff}, t_0}} \left(\frac{F_{\text{HE}}}{F_{\text{HE}, t_0}} \right)^{\alpha}, \quad (22)$$

to estimate the instantaneous expected number of muon neutrinos, at all other times t . Here, F_{HE} is the FAVA flux in the high-energy bin at time t , and F_{HE, t_0} the high-energy-bin FAVA flux at the time when the multi-wavelength SED was obtained. For α we assume $\alpha = 2.0$, which is typically expected in BL Lac objects in both in the SSC model, and in the presence of a sheath field, because in canonical models the proton luminosity increases simultaneously with the density of the target field during high-states ([Tavecchio et al. 2014](#); [Petropoulou et al. 2016](#); [Murase & Waxman 2016](#)).

³ Available online at <https://icecube.wisc.edu/science/data>

The ratio $A_{\text{eff},t}/A_{\text{eff},0}$ gives the relative exposure at a given time t , with respect to that at time t_0 , to allow for the possibility that the IceCube configuration changed during the time of the flare.

We further calculate the total expected number of neutrinos during the ten years that IceCube and *Fermi* have been in operation, integrating Equation 22 over the entire time-duration of the *Fermi* lightcurve.

In addition to IceCube, we consider the sensitivity of planned and proposed future neutrino telescopes to the expected signal from blazar neutrino flares. We consider the following future facilities (see Table B1 for abbreviations) which could form a future neutrino monitoring network (Resconi 2019):

- IceCube Gen2 (IceCube Collaboration 2014a). We assume that the extended IceCube detector will have an instrumented volume six times larger than IceCube in IC86 configuration.
- KM3NeT (KM3NeT Collaboration 2009). We assume that in its final configuration it will have an instrumented volume identical to that of IC86 but at latitude, $l = 32.27^\circ\text{N}$.
- Baikal-GVD (Baikal-GVD Collaboration 2018). We assume that in its final configuration it will have an instrumented volume identical to that of IC86, but at latitude, $l = 53.56^\circ\text{N}$.
- ONC (STRAW Collaboration 2019). We assume that in its final configuration, it will have an instrumented volume identical to that of IC86, at latitude, $l = 48.43^\circ\text{N}$.

For all four facilities, we further assume that the effective area as a function of energy and zenith angle is identical to that of IC86.

In order to calculate the number of neutrinos expected in the different detectors from identical blazar flares using Equation 21, we calculate the instantaneous zenith angle, θ , of a neutrino point source at declination δ , at time t , in a detector with acceptance uniform in right ascension, located at latitude l , using the expression,

$$\cos \theta = \sin \delta \cdot \sin l + \cos \delta \cdot \cos l \cdot \sin(2\pi t), \quad (23)$$

and obtain the time-averaged effective area as

$$A_{\text{eff}}(E_\nu, \delta, l) = \frac{1}{N} \sum_i^N A_{\text{eff}}(E_\nu, \theta_i, l), \quad (24)$$

where θ_i is the zenith angle of a source at declination δ as seen by a detector at latitude, l , at time-interval i , and the average, $A_{\text{eff}}(E_\nu, \delta, l)$ is obtained by summing over a large number, N , of time-bins.

4 RESULTS

Figures 3 and 4 show the expected neutrino flux from each flare in our sample for Normalisations A and B respectively. The peak neutrino energy-flux is expected at $\gtrsim 10$ PeV for Normalisation A and $\lesssim 1$ PeV for Normalisation B. The two figures show that the instantaneous neutrino flux is not strictly proportional to the photon flux at a particular wavelength since we have explicitly modelled the neutrino flux taking into account the physical parameters in each source.

The two most important source characteristics that contribute to a high expected instantaneous neutrino flux are

a high bolometric luminosity and a relatively low Doppler factor. These two conditions ensure a higher number density of target photons and $p\gamma$ interaction probability in the emitting region in the SSC model which follows from Equations 7 and 10. In addition, a higher bolometric luminosity and low Doppler factor imply a higher proton luminosity in the comoving frame. Within our model assumptions, these two conditions also lead to a higher neutrino flux for Normalisation B, where external Compton interactions occur, because we require that $u'_{\text{syn}} > u'_{\text{ext}}$ and $L_{\text{ext}} < L_{\text{syn}}$.

Tables 6 and 7 give the expected number of neutrinos in each flare in our sample in the IceCube detector, for Normalisation A and Normalisation B, respectively. We have calculated the expected number of neutrinos by integrating the neutrino spectrum above 100 TeV where the atmospheric background is low. The highest neutrino counts under Normalisation A are expected for AO 0235+164, which is the most luminous source in our sample, despite being the most distant, at redshift $z = 0.94$. In the case of Normalisation B, AO 0235+164 has been modelled with ξ_{cr} ten times lower than all other sources. The highest neutrino counts are expected in this case from AO 0235+164 and from the flares of OJ 287 and TXS 0506+056 which are some of the brightest sources in our sample.

Significantly lower neutrino counts are expected for the nearby HSP sources (Mrk 421, Mrk 501, 1ES 1959+65, PG 1553+113). These are generally less bright than the LSP/ISPs studied. PG 1553+113 is an exception among the HSPs we modelled because it is one of the brightest sources considered, however, it has a high Doppler factor and thus a low predicted neutrino luminosity.

In addition to sources having a high bolometric luminosity, high-neutrino counts can be expected for the longest γ -ray flares, for relatively nearby sources, and for sources located in a position in the sky favourable for detection within IceCube. Within the range of declinations spanned by the sources in our sample, in the $\sim 5^\circ - 72^\circ$ range, the effective area of IceCube in the direction of different sources varies in fact by up to a factor of 20.

The predicted neutrino event counts for Normalisation A are in general modest. Comparison with Table 7 reveals that the expected neutrino counts increase by up to three orders of magnitude for Normalisation B, due to the much higher baryon loading and neutrino production in interactions of protons with an external photon field.

It is interesting to note that the relative neutrino signal between the different flares is not the same under Normalisations A and B. For example, Mrk 501 produces the second strongest signal in our sample for Normalisation A, but a very weak neutrino flare in Normalisation B consistent with zero above 100 TeV. This is because Mrk 501, with detected variability of 4 hours, is assumed to have a small emitting region radius, r'_b , in our model. In the SSC model this increases the density of the relevant photon field for neutrino interactions significantly, whereas in the external-Compton model which generally dominates the SSC component as shown in Figure 4 the small r'_b implies a low proton maximum energy, such that the neutrinos produced in interactions of protons with the external photon field are very suppressed with respect to cases with a higher proton maximum energy.

If the same physical mechanism is in operation in TXS 0506+056 as in AO 0235+164 and OJ 287 and the pro-

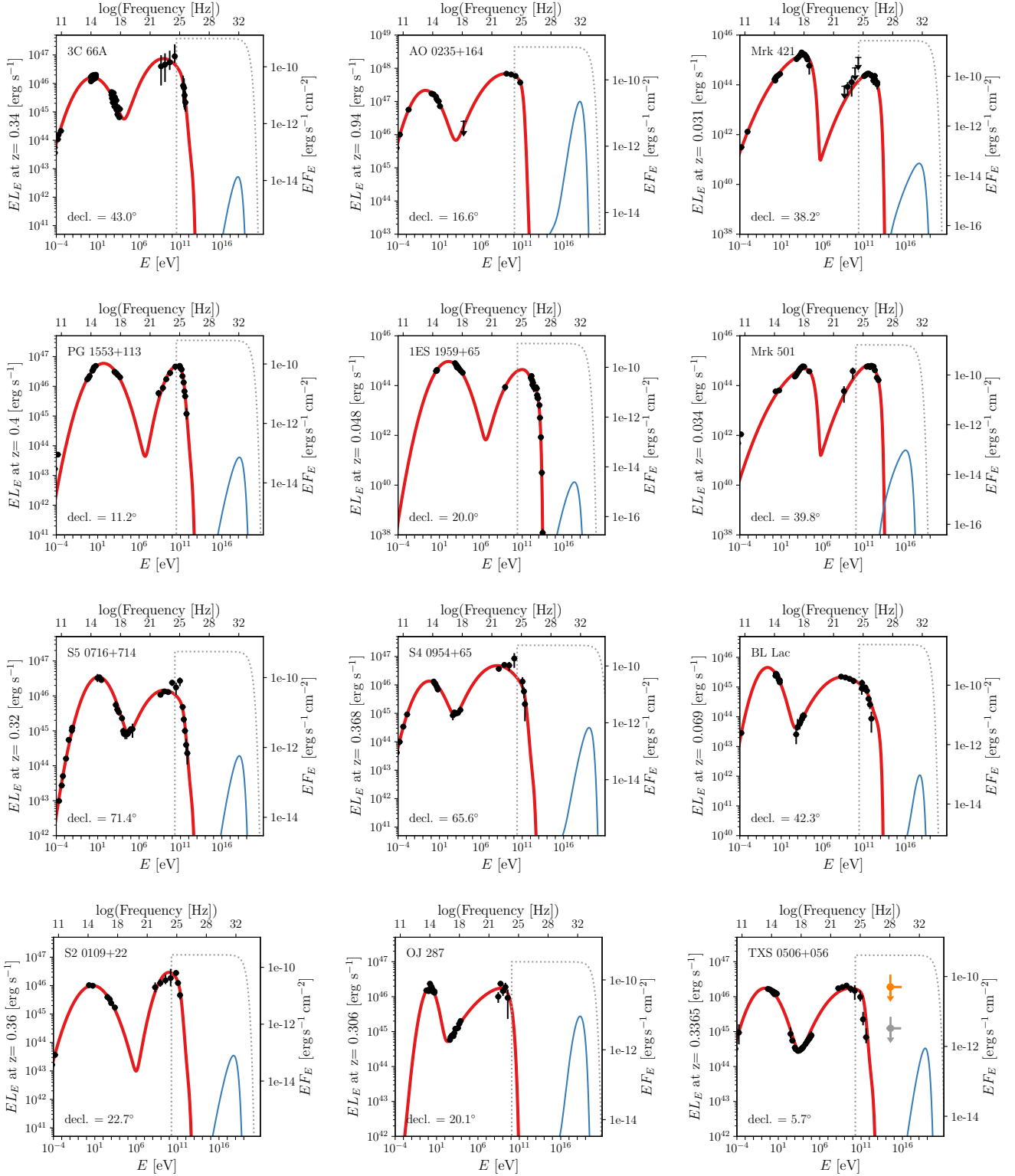


Figure 3. Broadband SED (red), injected proton flux (black dotted lines), and expected instantaneous neutrino flux (blue) for each for the flares in our sample in Normalisation A in the observer frame. Only neutrinos produced in the interactions of protons with photons in the accelerating region, assumed to be a spherical blob are shown. The cosmic rest frame luminosity for an observer at redshift equal to the redshift of each source is given on the left vertical axis. For TXS 0506+056, the data-points give the muon neutrino flux upper limits that would produce on average one detection like IceCube-170922A over a period of 0.5 (orange) and 7.5 years (grey) at the most probable neutrino energy as calculated in [IceCube Collaboration et al. \(2018\)](#).

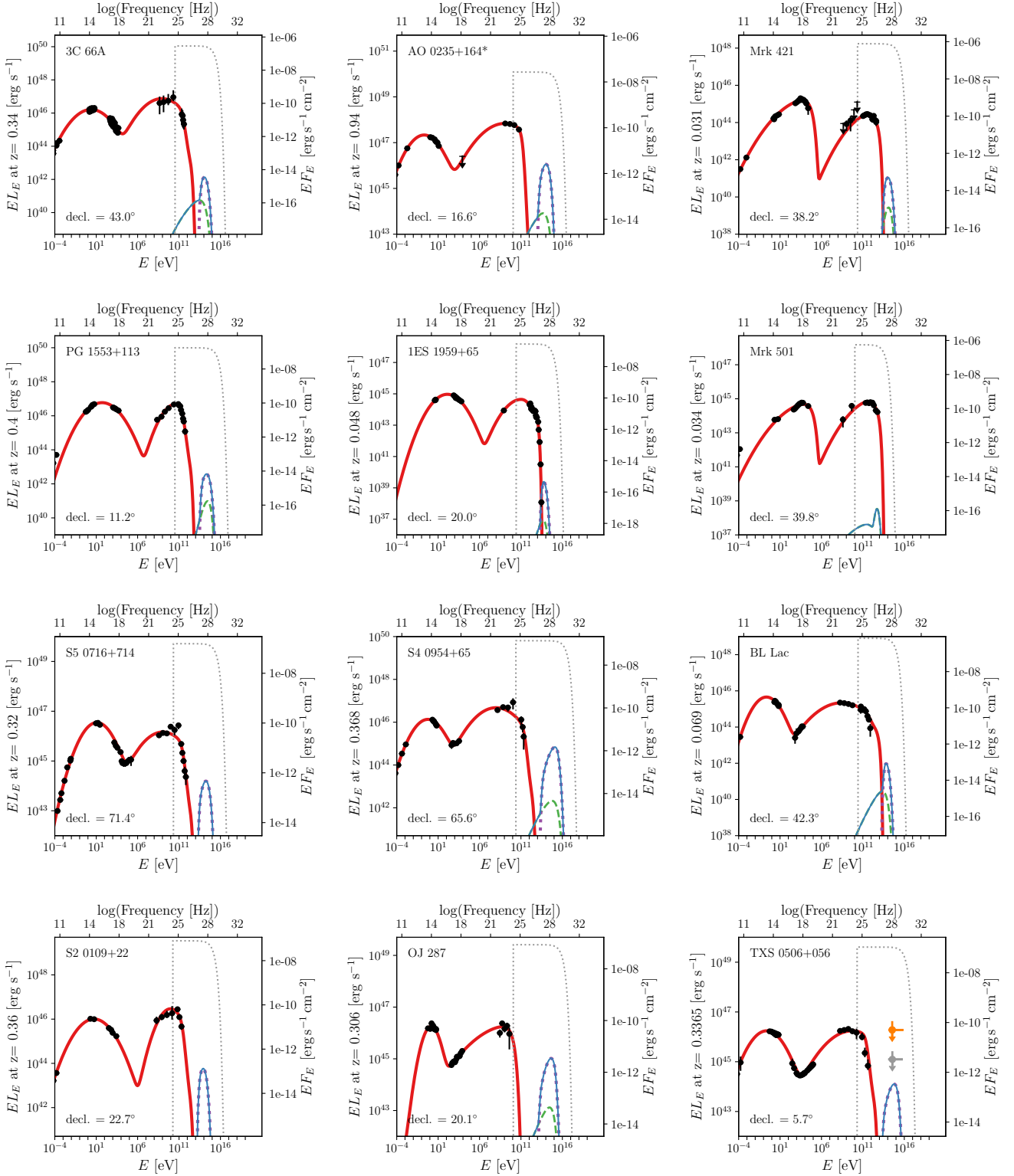


Figure 4. Same as Figure 3 but for Normalisation B. Green dashed lines give the neutrino emission produced in interactions of protons with photons the blob. For some of the SEDs these are very suppressed and not seen in the plots. Purple dotted lines give the neutrino flux produced in interactions of protons with photons of the stationary external field. Blue solid lines give the total neutrino emission. *The star marks that for AO 0235+164 we have used baryon loading ten times lower than all other sources, $\xi_{\text{cr}} = 150$.

Table 6. For each source the table gives the time duration of the studied flare in days ΔT , the declination, the assumed proton luminosity, \mathcal{L}_p^{46} , in units of 10^{46} erg s $^{-1}$ in the laboratory frame, the corresponding predicted laboratory frame muon-neutrino luminosity, $\mathcal{L}_{E\nu\mu}^{40}$, in units of 10^{40} erg s $^{-1}$, the predicted laboratory frame muon-neutrino energy output, $\mathcal{E}_{\nu\mu, \text{flare}}^{44, > 100 \text{ TeV}}$, in units of 10^{44} erg for the flare studied, and the corresponding number of predicted muon-neutrino archival events in IceCube, $N_{\nu\mu, \text{flare}}^{\text{IC}, > 100 \text{ TeV}}$ with energy ≥ 100 TeV for the model parameters of Normalisation A, which corresponds to baryon loading $\xi_{\text{cr}} = 10$, high maximum proton energy, and SSC scenario with no external photon fields. In addition, the number of muon neutrinos per year of flaring activity $N_{\nu\mu, \text{year flare}}^{\text{IC}, > 100 \text{ TeV}}$ is given. The three rightmost columns give the number of muon neutrinos produced during all the flares identified through the FAVA ten-year-lightcurve analysis, $N_{\nu\mu, \text{all flares}}^{\text{IC}, > 100 \text{ TeV}}$, the neutrino energy output of each source per average year, $\mathcal{E}_{\nu\mu, \text{yr}}^{44, > 100 \text{ TeV}}$, and the total number of expected neutrinos over the entire ten years of FAVA data available, $N_{\nu\mu, 10 \text{ yr}}^{\text{IC}, > 100 \text{ TeV}}$, in Normalisation A, under the assumption that $N_{\nu\mu} \propto F_{\text{HE}}^2$ (see Section 3.4 for details).

Source	ΔT	decl.	\mathcal{L}_p^{46}	$\mathcal{L}_{\nu\mu}^{40}$	$\mathcal{E}_{\nu\mu, \text{flare}}^{44, > 100 \text{ TeV}}$	$N_{\nu\mu, \text{flare}}^{\text{IC}, > 100 \text{ TeV}}$	$N_{\nu\mu, \text{year flare}}^{\text{IC}, > 100 \text{ TeV}}$	$N_{\nu\mu, \text{all flares}}^{\text{IC}, > 100 \text{ TeV}}$	$\mathcal{E}_{\nu\mu, \text{yr}}^{44, > 100 \text{ TeV}}$	$N_{\nu\mu, 10 \text{ yr}}^{\text{IC}, > 100 \text{ TeV}}$
3C 66A	14	43.0	700	400	1e+5	1e-8	2e-7	2e-7	1e+6	1e-6
AO 0235+164	84	16.6	9e+3	8e+6	2e+10	5e-4	2e-3	2e-3	1e+10	3e-3
Mrk 421	13	39.8	10	7	9e+2	3e-7	7e-6	6e-5	4e+4	1e-4
PG 1553+113	30	11.2	700	4e+3	1e+6	6e-6	5e-7	1e-5	2e+7	1e-4
1ES 1959+65	46	20.0	9	1	600	2e-7	1e-6	5e-7	100	8e-7
Mrk 501	21	38.2	7	30	4e+3	4e-5	7e-4	1e-3	2e+4	3e-3
S5 0716+714	14	71.4	400	2e+4	1e+6	2e-8	4e-7	6e-7	8e+6	1e-6
S4 0954+65	28	65.6	600	3e+4	7e+6	1e-7	1e-6	1e-7	1e+6	2e-7
BL Lac	7	42.3	50	70	1e+4	5e-7	2e-5	1e-5	7e+4	3e-5
S2 0109+22	21	22.7	200	3e+3	9e+5	5e-7	1e-5	2e-5	6e+6	4e-5
1ES 1959+65	84	20.0	4	3e-1	200	1e-7	5e-7	5e-7	100	8e-7
OJ 287	7	20.1	200	2e+5	2e+8	2e-5	1e-3	9e-5	3e+8	3e-4
TXS 0506+056	175	5.7	300	3e+4	2e+9	4e-5	7e-5	4e-5	4e+8	8e-5

Table 7. Same as Table 6 but for Normalisation B, which includes the expected number of neutrinos in interactions with an external photon field. *star superscripts denote that for AO 0235+164 we have used baryon loading factor ten times lower than all other sources $\xi_{\text{cr}} = 150$.

Source	ΔT	decl.	\mathcal{L}_p^{46}	$\mathcal{L}_{\nu\mu}^{40}$	$\mathcal{E}_{\nu\mu, \text{flare}}^{44, > 100 \text{ TeV}}$	$N_{\nu\mu, \text{flare}}^{\text{IC}, > 100 \text{ TeV}}$	$N_{\nu\mu, \text{year flare}}^{\text{IC}, > 100 \text{ TeV}}$	$N_{\nu\mu, \text{all flares}}^{\text{IC}, > 100 \text{ TeV}}$	$\mathcal{E}_{\nu\mu, \text{yr}}^{44, > 100 \text{ TeV}}$	$N_{\nu\mu, 10 \text{ yr}}^{\text{IC}, > 100 \text{ TeV}}$
3C 66A	14	43.0	1e+5	70	1e+4	5e-6	1e-4	5e-5	1e+5	5e-4
AO 0235+164	84	16.6	1e+5*	8e+5*	5e+8*	3e-2*	1e-1*	1e-1*	3e+8*	2e-1*
Mrk 421	13	39.8	2e+3	5	6e+2	6e-5	1e-3	1e-2	3e+4	3e-2
PG 1553+113	30	11.2	1e+5	200	6e+4	4e-5	5e-4	7e-4	8e+5	6e-3
1ES 1959+65	46	20.0	1e+3	8e-2	3e+1	3e-7	2e-6	8e-7	10	1e-6
Mrk 501	21	38.2	1e+3	2e-2	2	0	0	0	20	0
S5 0716+714	14	71.4	6e+4	1e+4	2e+6	3e-4	8e-3	1e-2	1e+7	2e-2
S4 0954+65	28	65.6	9e+4	6e+4	2e+7	9e-4	1e-2	1e-3	3e+6	1e-3
BL Lac	7	42.3	8e+3	40	8e+3	5e-5	2e-3	1e-3	4e+4	2e-3
S2 0109+22	21	22.7	4e+4	3e+3	7e+5	3e-4	6e-3	1e-2	5e+6	2e-2
1ES 1959+65	84	20.0	700	2e-2	20	2e-7	7e-7	8e-7	10	1e-6
OJ 287	7	20.1	3e+4	8e+4	4e+7	4e-2	2	2e-1	7e+7	7e-1
TXS 0506+56	175	5.7	5e+4	2e+4	2e+7	2e-2	4e-2	2e-2	5e+6	4e-2

ton content in these sources is the same, one expects a stronger signal from these two past flares in the archival IceCube data than in the 2017 flare of TXS 0506+056. However, the expected number of neutrinos is below the sensitivity of IceCube even in Normalisation B. Therefore, even in the absence of neutrino signal from these two flares, it is not possible to constrain this model.

Comparison of time integrated neutrino flux column, $N_{\nu\mu, 10 \text{ yr}}^{\text{IC}, > 100 \text{ TeV}}$, on Tables 6 and 7 with the flux produced by a single flare, $N_{\nu\mu, \text{flare}}^{\text{IC}, > 100 \text{ TeV}}$, reveals that under our assumed relation between L_ν and L_γ a short neutrino flare can produce a sizeable fraction of the time-integrated flux of a neutrino emitting blazar. In the case of S4 0954+65 the 40-fold flux enhancement as seen in the FAVA data, means that \sim half the expected neutrino flux from this source in the last ten years comes from the 28-day window around the 2015 flare. This is also true for the 2017 flare of TXS 0506+056.

Tables 6 and 7 also give the required cosmic-rest-frame proton luminosity \mathcal{L}_p during the flares in our model. After converting it to the absolute beaming-corrected proton luminosity, $\mathcal{L}_p/2\Gamma^2$, this can be compared to the Eddington luminosity for a sanity check. Assuming a typical black-hole mass of $10^{8.5} M_\odot$ (Plotkin et al. 2011), while with Normalisation A, all proton luminosities are safely below the Eddington limit, with Normalisation B we find that the beaming-corrected proton luminosity is in the range $\sim 0.2 - 30$ times the Eddington luminosity. This is not necessarily problematic, as during outbursts the Eddington limit can be temporarily exceeded (e.g. Sadowski & Narayan 2015).

In Figure 5, the expected number of muon neutrinos in IceCube in full configuration (IC86) is contrasted with the number of muon neutrinos that would have been detected for the studied flares in planned future neutrino facilities. Our assumptions about the effective area of these future de-

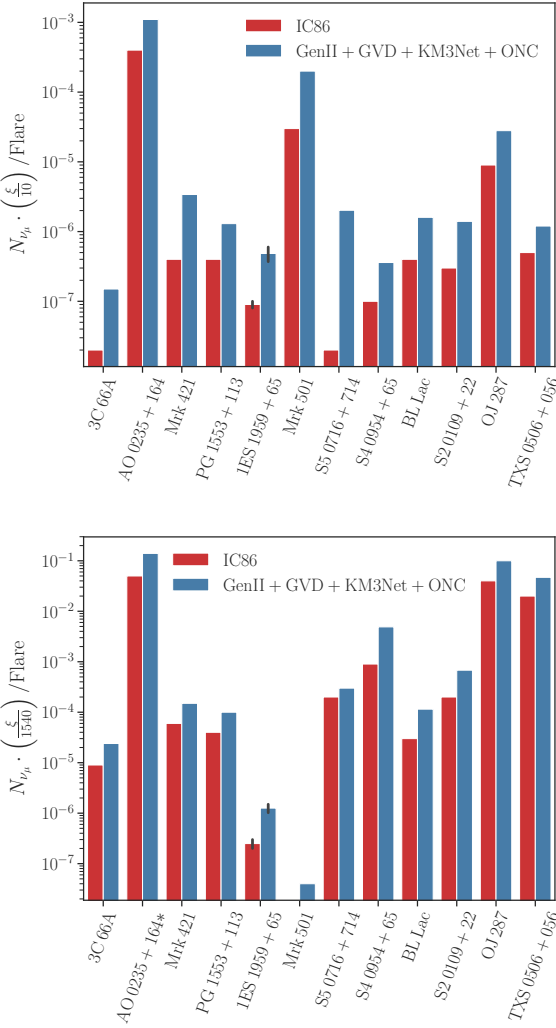


Figure 5. Predicted neutrino counts for each of the flares in our sample under the Normalisation A (top) and Normalisation B parameters (bottom). The red bars give the expected number of muon neutrinos as seen in IceCube, in the IC86 configuration, and comparison to the expected number of neutrinos for identical flares if GenII, GVD, ONC, and KM3Net are in operation. For IES 1959+650 the error bars are statistical and derive from the modelling of two separate flares. *The star marks that for AO 0235+164 we have used baryon loading ten times lower than all other sources, $\xi_{\text{cr}} = 150$.

tectors are presented in Section 3.4. The number of expected neutrinos is given as a function of the baryon loading factor, which could be as much as one order of magnitude higher assuming Normalisation A as discussed in Section 3.1. For the sources with high positive declination future neutrino detectors in the Northern hemisphere will strongly increase the expected neutrino counts from individual flares as demonstrated by the case of S5 0716+714.

Figure 6 shows a sky map of the energy released in muon neutrinos, $\mathcal{E}_{\nu_{\mu}, > 100 \text{ TeV}}^{\text{fl}} / \nu_{\mu, \text{flare}}$, during each of the flares in our sample under the assumptions of Normalisations A and B, in equatorial projection. The size of the circles is proportional to the number of neutrinos expected in each flare. Comparison of the same source across two plots, reveals that in some

cases the expected energy flux is larger assuming Normalisation A while more neutrinos are expected from Normalisation B. When this is the case, it is because the $E_{\nu} F_{E_{\nu}}$ neutrino energy flux with Normalisation A continues to increase up to higher energies as illustrated in Figure 3, but the expected number of neutrinos depends on the $F_{E_{\nu}}$ flux, which peaks at lower energies for some of the sources.

The bulk of the neutrino flux from blazar flares in our formalism is expected at energies larger than 100 TeV where the atmospheric neutrino background is low (IceCube Collaboration 2016c). Constraining the search for blazar-flare neutrinos to energies greater than 100 TeV, where the search is approximately background free, a future neutrino detector can constrain the baryon-loading factor of the jet to be,

$$\xi_{\text{cr}} \leq \frac{N_{\text{FC}}^{90} \cdot \xi_0}{\sum_{\text{source } i} N_{\nu_{\mu}}^i}, \quad (25)$$

where $N_{\text{FC}}^{90} = 2.44$ is the Feldman-Cousins upper limit at 90% confidence, in the absence of neutrino signal, for a background free search, and ξ_0 the assumed baryon loading factor to obtain $N_{\nu_{\mu}}^i$, the number of expected muon neutrinos from flaring periods for the i th source.

In our conservative model (Normalisation A), the flare-only neutrino signal is too low to be constrained by Gen2+GVD+KM3Net+ONC or similar detectors, and time-integrated searches for neutrino signal from BL Lacs are preferable.

Assuming Normalisation B, for the two most powerful neutrino emitters in our sample, AO 0235+164 and OJ 287 (scaled down in the case of AO 0235+164, with $\xi_{\text{cr}} = 150$ to bring the cascade to a non-detectable level), a future neutrino network with effective volume ten times larger than IC86, (denoted $\text{IC} \times 10$) with the exposure of Gen2+GVD+KM3Net+ONC would detect $N_{\nu_{\mu}, \text{all flares}, > 100 \text{ TeV}}^{\text{IC} \times 10, 10 \text{ yr}} \approx 3$ with our flare-period selection based on the HE FAVA data. In the absence of the muon-neutrino signal, assuming a flare pattern identical to that of the past decade, the baryon loading will be constrained to $\xi_{\text{cr}} < 1250$ if the energy density of the external photon target field can be probed. Aggressively reducing the energy threshold to 40 TeV, which would bring the background up to an acceptable level of $N_{\text{bg}} \approx 0.2$, assuming the background model of IceCube Collaboration (2016c), we would expect $N_{\nu_{\mu}, \text{all flares}, > 40 \text{ TeV}}^{\text{IC} \times 10, 10 \text{ yr}} \approx 5$ or limit $\xi_{\text{cr}} \lesssim 835$.

For a larger number of such powerful sources the constraint on ξ_{cr} scales down linearly with the number of expected neutrinos following Equation 25. To illustrate the possible reach of future instruments we use the 34 BL Lac objects extracted from the 1-Jy catalogue (Stickel et al. 1991; Kuehr et al. 1981). For these sources, which are predominantly LSPs, the “bolometric” luminosity of the synchrotron peak, $L_{\text{S,bb}}$, scales approximately as their radio luminosity.⁴ We make use of this approximate relation. Using the radio flux at 5 GHz, $F_{5 \text{ GHz}, i}$, we find that for an assumed scaling of the neutrino luminosity as $L_{\nu} \propto L_{\text{S,bb}}^{\alpha}$, each source,

⁴ This is the case for LSP objects because the peak of the synchrotron emission lies in the frequency range $10^{12} - 10^{14}$ Hz. Given this small range, one can extrapolate almost linearly between the radio flux and the flux at the synchrotron peak

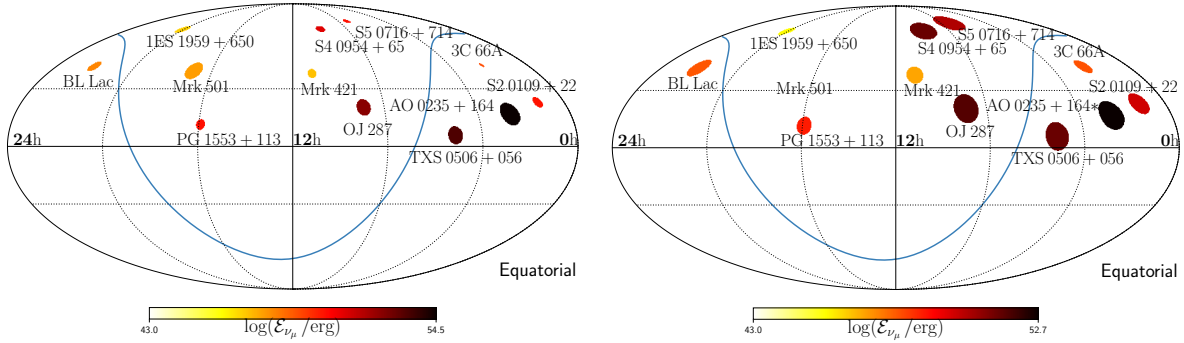


Figure 6. Left: Predicted per-flavour neutrino energy output during the studied flare with Normalisation A. The size of the circles is proportional to the number of neutrinos expected in each flare. For flares that occurred prior to 2011, the appropriate incomplete IceCube configuration is taken into account. The blue solid line marks the Galactic plane. Right: Same as on the left but for Normalisation B. *The star marks that for AO 0235+164 we have used baryon loading ten times lower than all other sources, $\xi_{\text{cr}} = 150$.

i , would produce of order,

$$N_{\nu_\mu}^i \sim N_{\nu_\mu}^{\text{OJ287}} \left(\frac{F_{5\text{ GHz},i}}{F_{5\text{ GHz},\text{OJ287}}} \right)^\alpha \frac{A_{\text{eff},i}}{A_{\text{eff},\text{OJ287}}} \quad (26)$$

muon neutrinos if it had an identical flare profile and neutrino spectrum to that of OJ 287. In 10 years of observations with Gen2+ONC+GVD+KM3NeT, for $\alpha = 2$ which we have assumed throughout this work, the stacked number of expected neutrinos from the 1-Jy BL Lacs would be $N_{\nu_\mu, \text{all flares}, > 100 \text{ TeV}}^{\text{IC} \times 10, 10 \text{ yr}} \approx 22$ or otherwise constrain the baryon loading factor of these sources to $\xi_{\text{cr}} < 170$. The limits on ξ_{cr} can be improved by increasing the number of sources and/or by stacking longer duration flares. Meanwhile, X-ray and proposed MeV γ -ray telescopes will provide complementary measurements or constraints to the baryon loading factor of blazars by monitoring the part of the SED where the secondary cascade emission is expected.

It is interesting to note that the FAVA lightcurve of AO 0235+164 shows another \sim year-long flare in 2015. The IceCube data for this time are not publicly available and could not be examined. It has not escaped our attention that the Very high-energy Gamma-ray follow-up (GFU) program of IceCube events registered a neutrino triggered alert in April 2015 from the direction of AO 0235+164 (IceCube Collaboration 2016a). The GFU alerts are produced only in response to an excess of neutrinos in the direction of the source and are by construction independent of any electromagnetic flaring activity. The time of the alert with respect to the FAVA lightcurve is illustrated in Figure A1. AO 0235+164 is one of the ~ 100 monitored sources within the GFU program, and the alert was triggered by the observation of eight neutrinos within 16.4 days. An alert with such significance is expected at a rate $\sim 0.01/\text{source}/\text{year}$, and is thus consistent with background expectations, even after accounting for the independent observation that it was flaring in the FAVA analysis.

We have modelled the FAVA flare as a double gaussian with duration ≈ 444 days. Assuming that the SED of AO 0235+164 was in the same state on MJD 57427, which is when the source reached peak flux in the FAVA data, as it had been on MJD 54736, which is our fitted peak of the 2008 flare, we can obtain an estimate of the neutrino signal from

this flare, following the procedure outlined in Section 3.4, which turns out to be $N_{\nu_\mu, > 100 \text{ TeV}} \approx 4 \cdot 10^{-4} (\xi_{\text{cr}}/10)$ with Normalisation A, and $N_{\nu_\mu, > 100 \text{ TeV}} \approx 0.05 (\xi_{\text{cr}}/150)$ with Normalisation B.

4.1 Systematic uncertainties

The expected neutrino flux from a blazar flare is extremely sensitive to the Doppler factor of the motion of the emitting region of the blazar jet. As demonstrated in Section 3, in the blob formalism the observed neutrino luminosity is amplified by a factor of δ^4 with respect to the emitted neutrino luminosity. The Doppler factor of the motion of the emitting region can be constrained by blazar observables such as the time variability, and the requirement that the source is not opaque to emitted γ -rays, but the most detailed measurements of jet kinematics come from radio galaxy observations (Jorstad et al. 2017; Lister et al. 2019). In the SSC scenario, additionally, the magnetic field can be uniquely specified for a given value of δ in the absence of measurement uncertainties. The value of B relates to the maximum energy of protons, and determines the balance between cooling timescales in the emitting region and thus also the shape of the emerging neutrino spectrum.

At present, there exist large uncertainties in the determination of the Doppler factor, Lorentz factor, and viewing angle of individual blazar jets, though future jet observations may narrow down the allowed parameter region. Broadly speaking the bulk of BL Lac jets are expected to have Doppler factors in the range $10 \leq \delta \leq 50$ (Hovatta et al. 2009; Lioudakis & Pavlidou 2015). Typically, for an individual blazar SED an uncertainty range can only be quoted within an assumed model for the emission from the source in question. The addition of free parameters, including more than one emitting region and external photon fields, makes it even more challenging to specify δ and B .

A final parameter of importance for the expected number of neutrinos, once δ and B are specified, is the baryon loading factor ξ_{cr} . This can be constrained with neutrino or X-ray observations once δ and B are measured as detailed in the previous section. In what follows we explore the effect of systematic uncertainties on δ and B on the expected number

of neutrinos from individual blazar flares for fixed $\xi_{\text{cr}} = 10$, and other model parameters fixed as per Normalisation A.

The upper panel of Figure 7 illustrates the parameter space allowed for δ and B from the SED of 3C 66A during its 2008 flare. For each investigated combination of δ and B we fit the SED of 3C 66A using Equations 1 and 2, for fixed values of δ , B and $t_{\text{var,d}}$. We perform a numerical scan over δ and B , calculating the χ^2 of every fit. The SED fits are done with the log-parabolic model presented in Section 3.3. The colormap on the upper panel of Figure 7 gives the deviation of the fitted SED with respect to the best-fit SED in units of,

$$n\sigma = S\sqrt{\chi^2 - \chi_{\text{min}}^2} \quad (27)$$

with χ_{min}^2 the χ^2 of the best-fit realisation. The scale factor $S = 1/\sqrt{\chi_{\text{min}}^2/\text{ndf}}$, where ndf the number of free parameters of the fit, is an approximate correction (Rosenfeld 1975) to enlarge the uncertainty because of a poor minimum χ^2 that might either signify underestimated experimental uncertainties or simplified model assumptions. Equation 27, defines the confidence regions illustrated in Figure 7 in units of standard deviations. The precise meaning of the plotted confidence regions is that the 1σ contour gives the 68.3% containment region of δ at a fixed value of B and vice versa, assuming that the two variables are normally distributed (James 2006). The contour lines in Figure 7 give the number of standard-deviations with respect to the best-fit SED. The red cross gives the literature value of δ and B assumed throughout the rest of this work, as summarised in Table 4.

The lower panel of Figure 7 gives the expected number of muon neutrinos from the flare of 3C 66A, with Normalisation A, while scanning over δ and B , integrated over neutrino energies above 100 TeV. We fix the SED here to the best-fit SED, and vary only δ and B i.e. we do not simultaneously investigate the effect of the variation of the shape of the target photon field, which we expect to be subdominant.

Note that unlike in all earlier sections we have not calculated the number of expected neutrinos using Equation 22 but instead use the box approximation, i.e.,

$$N_{\nu} = \frac{dN_{\nu,t_0}}{dt} \cdot \Delta T, \quad (28)$$

with $dN_{\nu,t_0}/dt$ given by Equation 21, and ΔT the time duration of the *Fermi* flare given in Table 5. Figures 8, and 9 give the same results but for the flares of S5 0716+714 and S2 0109+22.

Within the 1σ error-region of 3C 66A which has a long and shallow minimum the neutrino expectation varies by more than four orders of magnitude. For this source the best χ^2 in the log-parabolic model is outside the figure bounds at $\delta = 93$ and $B = 0.001$ G. For S5 0716+714 the literature value estimate is about $\sim 4\sigma$ away from the best-fit estimate obtained with the log-parabolic model, and in this case the expected number of neutrinos in these two models varies by ~ 1.5 orders of magnitude. For S2 0109+22 the literature value falls 3σ away from the best-fit log-parabolic parameters. In this case also the expected number of neutrinos in the two models varies by ~ 1.5 orders of magnitude. It is important to note that additional constraints beyond the shape of the SED investigated here can be imposed to ex-

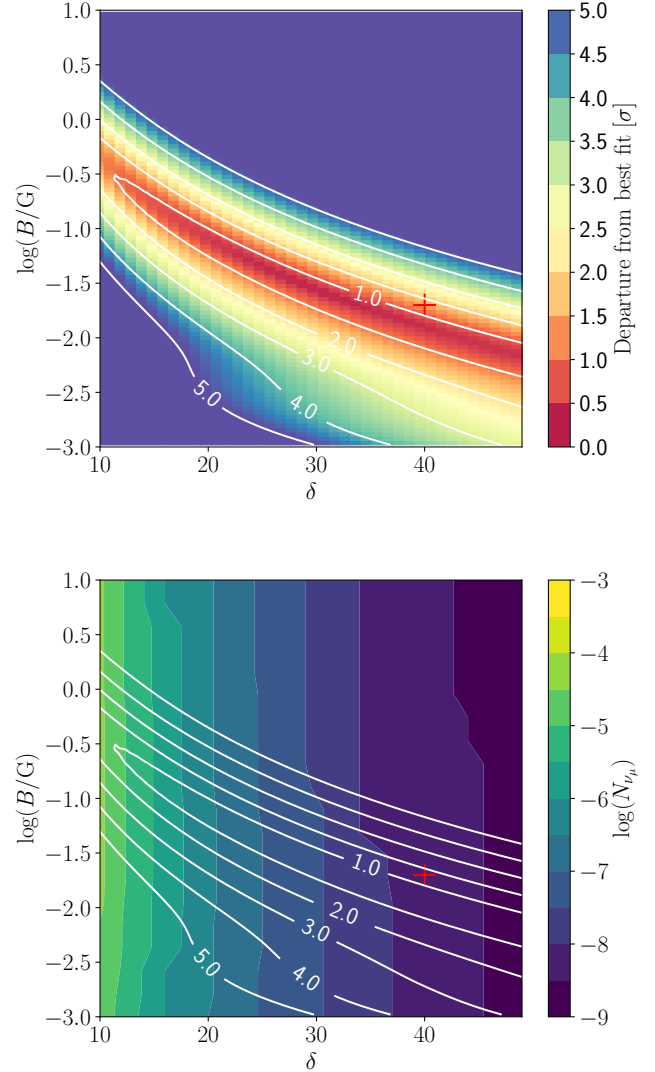


Figure 7. Top: Systematic uncertainty on the determination of δ and B (in Gauss) during the 14-day, October 2008 flare of 3C 66A. The colormap gives the departure from the best fit in units of σ (see main text for details), i.e. realisations with departure $\leq 2\sigma$ encompass the 95% allowed region assuming a Gaussian distribution. Bottom: Number of muon neutrinos expected to be seen in IceCube (IC86) for each combination of δ and B . The red cross (in top and bottom panels) marks the values of δ and B assumed in the present study.

clude certain regions of the parameter space shown in these plots; for example, rapid variability may impose a limit on the Doppler factor of the source on a case by case basis. Here, our aim is simply to illustrate the strong dependence of the neutrino flux expectations on the physical conditions inside the source and the model dependence of the derived values of these parameters.

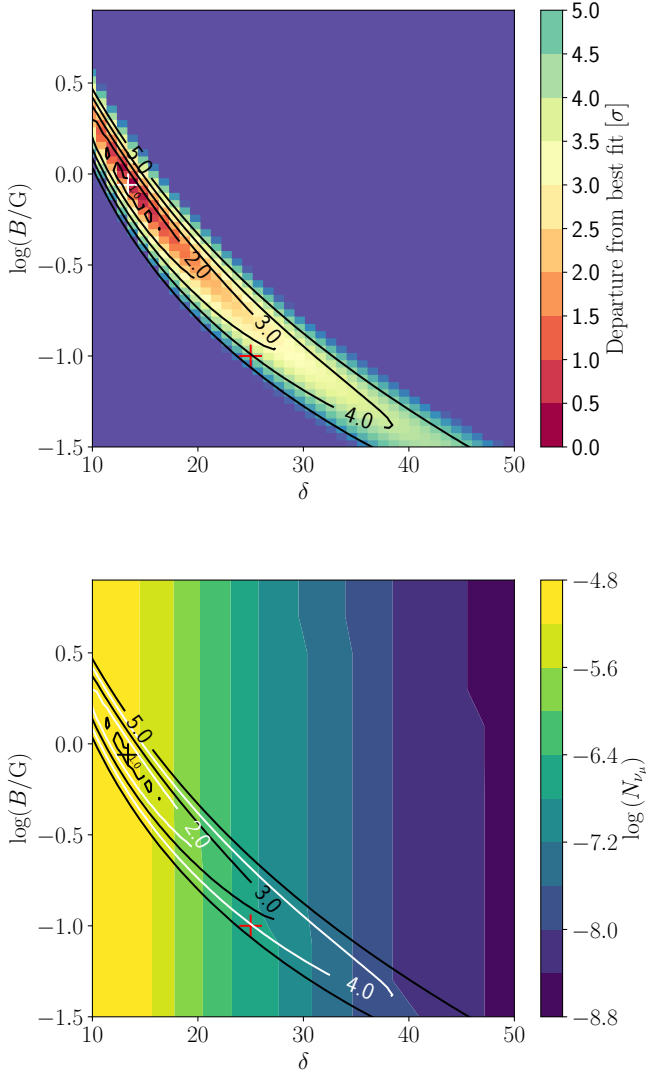


Figure 8. Same as Figure 7 but for the 14-day January 2015 flare of S50716+714. The white (black) cross marks the values of δ and B that give the best-fit χ^2 in the top (bottom) panel.

5 DISCUSSION AND CONCLUSIONS

We have studied the expected number of neutrinos from individual blazar flares, focusing on BL Lac objects. We presented the expected number of neutrinos from past flares from twelve sources that were detectable by IceCube. We employed a model based on the SSC formalism to keep the number of free parameters minimal. We considered a broad range of the allowed parameter space for the efficiency of proton acceleration in BL Lac jets, the jet baryon loading, and the presence of external fields. To model the expected neutrino fluence of each of the flares from the twelve sources studied we used simultaneous multi-wavelength observations of the SEDs of the sources. We used the FAVA lightcurves to homogeneously define the duration of the flares.

We calculated the expected number of high-energy neutrinos from each of the flares, under conservative and opti-

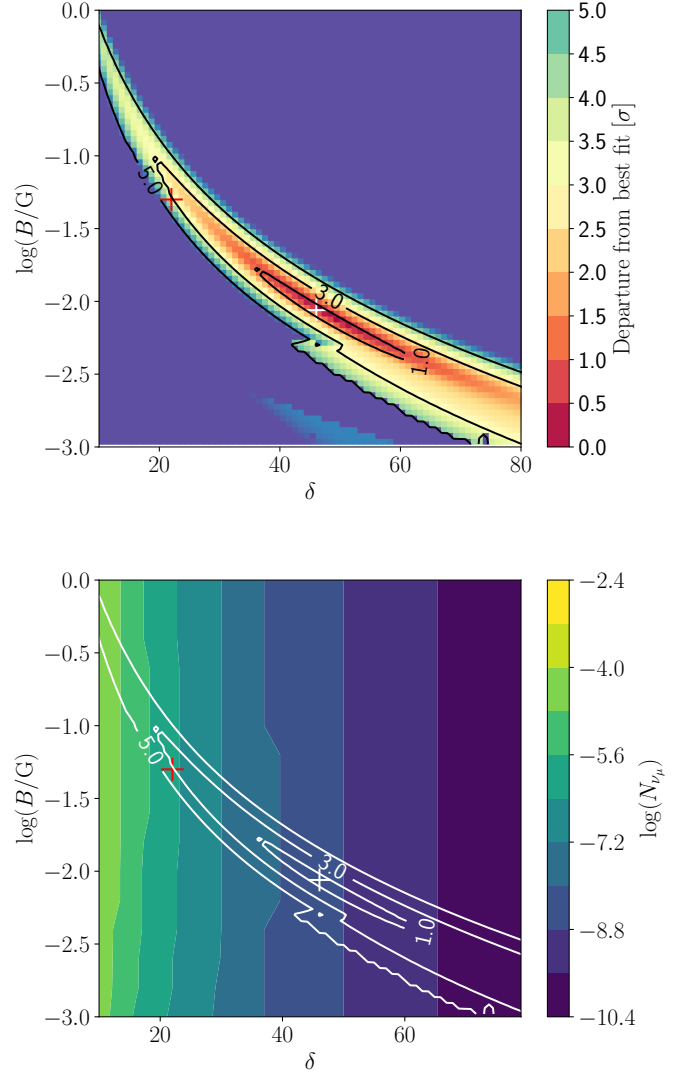


Figure 9. Same as Figure 7 but for the 21-day July 2015 flare of S20109+22. The white cross marks the values of δ and B that give the best-fit χ^2 .

mistic assumptions, with the aim to address the question of what are the characteristics that make a flare particularly strong in terms of expected neutrino counts, and whether the origin of neutrinos in γ -ray bright blazar flares, which is suggested by the 2017 observations of TXS 0506+056, is further testable with future neutrino observations.

We found that, in general, the largest neutrino signal is expected from the flares of the most luminous sources, as long as they have moderate Doppler factors. In this sense, the neutrino flux is dominated by the most powerful sources/flares, and thus given the rarity of BL Lac objects the expected neutrino signal in stacked searches does not increase significantly by including faint sources/flares.

In the context of the SSC model, under conservative assumptions about the baryon loading of BL Lac jets, $\xi_{\text{cr}} \sim 10$, which corresponds to the average jet baryon loading expected if the diffuse UHECR flux is powered by blazars, and

assuming the only available target photon field for neutrino interactions is the photon-field comoving with the emitting region, the expected number of muon neutrinos in IceCube per flare is low, $N_{\nu_{\mu}, > 100 \text{ TeV}} \lesssim 5 \cdot 10^{-4}$. The stacked signal over ten years of flare-periods for the most powerful sources in our sample is also low $N_{\nu_{\mu}, 100 \text{ TeV}}^{\text{IC}, 10 \text{ yr}} \lesssim 10^{-3}$. If such a mechanism is exclusively in operation, we do not expect a strong neutrino signal in stacked searches for neutrinos from blazar γ -ray flares even with an order of magnitude larger neutrino detector.

Under optimistic assumptions about the jet proton luminosity and in the presence of external photon fields, inspired by the modelling of the 2017 flare of TXS 0506+056, we found that the two most powerful sources in our sample, AO 0235+164 and OJ 287 would produce, in total, $N_{\nu_{\mu}, \text{all flares}, > 100 \text{ TeV}}^{\text{IC} \times 10, 10 \text{ yr}} \approx 3$ muon neutrinos, during *Fermi* flaring periods, in future neutrino detectors with total instrumented volume \sim ten times larger than IceCube, or otherwise lead to a constraint on the proton luminosity of blazar jets, $\xi_{\text{cr}} \lesssim 1250$. Stronger constraints on the baryon loading can be obtained with the addition of more powerful sources or by lowering the energy threshold of the neutrino search at the cost of additional atmospheric neutrino background. We illustrated the expected reach of constraints on the jet proton luminosity with a stacking approach using the 1-Jy BL Lac sample. In all instances, for such a constraint, the energy density of the external field, Doppler factor, and magnetic field strength in the emitting region need to be independently determined.

We demonstrated that the main uncertainties in predicting the neutrino output from individual flares are the Doppler factor of the motion of the jet emitting region, the magnetic field strength, the presence of external target photon fields, and the baryon content of the jet. We studied the systematic uncertainty in the expected neutrino flux from individual blazar flares introduced by the uncertainty of δ and B . We found that δ and B can vary a significant amount, even in the relatively well constrained SSC model, and within this uncertainty range the expected number of neutrinos also varied by up to ~ 2 orders of magnitude for the flares that we studied. The Doppler factor, magnetic field strength, and presence of external photon fields, can be constrained by radio, γ -ray and other astronomical observations. With these parameters specified, future neutrino detectors will be able to constrain or measure the baryon loading of blazar jets. Thus, astronomical observations are of paramount importance for understanding neutrino production in blazars.

Further to the two benchmark models we studied, and the systematic uncertainty on δ and B , there are two ways to increase the neutrino production in the studied flares:

- (i) increase the baryon loading
- (ii) increase the energy density of the stationary field.

In general, the baryon loading cannot be increased arbitrarily because of the associated electromagnetic cascade emission expected from the interactions of the protons, which would alter the shape of the observed SED. For some of the SEDs we studied there is room to increase the baryon loading with respect to our optimistic benchmark Normalisation B, but blazars with such strong baryon loading are not expected to be typical. Firstly, the radiative feature that

would be produced in the \sim keV-MeV energy range of the SED (as in e.g. Figure 1 of Petropoulou & Mastichiadis 2015) is not broadly observed. The strong upper limits on the baryon loading factor on this source-by-source basis, were demonstrated extensively during the follow-up campaign of the 2017 flare of TXS 0506+056. Additionally, if all blazar jets had such strong baryon loading, they would overproduce the observed cosmic ray spectrum and the diffuse γ -ray background measured by *Fermi*, since very-high and ultra-high-energy cosmic rays produce γ -ray cascades during their intergalactic propagation (e.g. Murase et al. 2012b).

With regard to item (ii) we have only investigated scenarios where $u'_{\text{syn}} > u'_{\text{ext}}$. This is not necessarily the case. However, for most of our sources, which emit TeV γ -rays, the external radiation field energy density cannot be much higher than we investigated here in a one-zone setup, or the opacity to TeV γ -rays would be too large to allow the observed γ -rays to escape. An additional constraint on the energy density of any external radiation field in BL Lac objects comes from the relative strength and peak frequency of the two bumps of the SED (Tavecchio et al. 2019). In the case of HSP objects the upper limit on u'_{ext} is often stronger than the constraint imposed by requiring transparency to TeV photons, and generally $u'_{\text{ext}} \leq 10 \cdot u'_{\text{syn}}$ can be considered a generous upper limit. In summary, neutrino production cannot be systematically larger than we have investigated in this work in a one-zone model.

We did not study FSRQ objects explicitly, though our sample contains sources which are intrinsically FSRQs. These will be the subject of subsequent work. Being more powerful, with stronger external fields, FSRQs likely can produce more neutrinos per flare for similar values of the baryon loading factor. On the other hand, since the SSC mechanism is likely not in operation in FSRQs, the number of free parameters needed to model neutrino production is larger, and the model parameters less well constrained. It is also possible that there are systematic differences in the proton content of BL Lac and FSRQ jets as shown in e.g. Croston et al. (2018).

A key ingredient for future neutrino analyses to be able to constrain, or in the case of neutrino detection in coincidence with blazar flares, determine the properties of the sources, such as the baryon loading of the jet, is the availability of a simultaneous multi-wavelength observations of the spectral energy distribution at the time of the flare, and determination of the Doppler factor and magnetic field of the jet from precise astronomical observations.

ACKNOWLEDGEMENTS

We thank Jaime Alvarez-Muñiz, Rolf Buehler, Matteo Ceruti, Yu-Ling Chang, Theo Glauch, Paolo Giommi, Shigeo Kimura, Ioannis Myserlis, Maria Petropoulou, Andrew Taylor and Michael Unger for useful discussions. This work is supported by the Deutsche Forschungsgemeinschaft through grant SFB 1258 “Neutrinos and Dark Matter in Astro- and Particle Physics” (F.O., P.P., E.R.), the Alfred P. Sloan Foundation and NSF grant No. PHY-1620777 (K.M.) and the Eberly Foundation (P.M.)

REFERENCES

- Ackermann M., Bernardini E., Hauschildt T., Reaconi E., 2005, in *Proceedings of ICRC 2005*.
- Ahlers M., Halzen F., 2018, *Prog. Part. Nucl. Phys.*, 102, 73
- Atoyan A., Dermer C. D., 2001, *Phys.Rev.Lett.*, 87, 221102
- Atoyan A. M., Dermer C. D., 2003, *ApJ*, 586, 79
- Baikal-GVD Collaboration 2018. ([arXiv:1808.10353](#))
- Baring M. G., 2006, *ApJ*, 650, 1004
- Berezinsky V., Gazizov A. Z., Grigorieva S. I., 2006, *Phys. Rev. D*, 74, 043005
- Bonning E., et al., 2012, *ApJ*, 756, 13
- Böttcher M., 2005, *ApJ*, 621, 176
- Carrasco L., Porras A., Recillas E., Chavushyan V., Carraminana A., 2015, *The Astronomer's Telegram*, 8044
- Cerruti M., Zech A., Emery G., Guarini D., 2017, *AIP Conf. Proc.*, 1792, 050027
- Cerruti M., Zech A., Boisson C., Emery G., Inoue S., Lenain J. P., 2019, *MNRAS*, 483, L12
- Chandra S., Zhang H., Kushwaha P., Singh K. P., Bottcher M., Kaur N., Baliyan K. S., 2015, *ApJ*, 809, 130
- Ciprini S., 2015, *The Astronomer's Telegram*, 7975
- Costamante L., Cutini S., Tosti G., Antolini E., Tramacere A., 2018, *MNRAS*, 477, 4749
- Croston J. H., Ineson J., Hardcastle M. J., 2018, *MNRAS*, 476, 1614
- D'Elia V., Padovani P., Giommi P., Turriziani S., 2015, *MNRAS*, 449, 3517
- Danforth C. W., Keeney B. A., Stocke J. T., Shull J. M., Yao Y., 2010, *ApJ*, 720, 976
- Danforth C. W., Nalewajko K., France K., Keeney B. A., 2013, *ApJ*, 764, 57
- Dermer C. D., Murase K., Takami H., 2012, *ApJ*, 755, 147
- Dermer C. D., Murase K., Inoue Y., 2014, *JHEAp*, 3-4, 29
- Dimitrakoudis S., Petropoulou M., Mastichiadis A., 2014, *Astropart. Phys.*, 54, 61
- Fermi-LAT Collaboration 2009, *ApJ*, 697, 1071
- Fermi-LAT Collaboration 2010a, *ApJ*, 716, 30
- Fermi-LAT Collaboration 2010b, *ApJ*, 722, 520
- Fermi-LAT Collaboration 2011, *ApJ*, 743, 171
- Fermi-LAT Collaboration 2017, *ApJ*, 846, 34
- Fermi-LAT Collaboration, VERITAS Collaboration, GASP-WEBT Consortium, et al., 2011, *ApJ*, 726, 43
- Fermi-LAT Collaboration, Moderski R., Nalewajko K., Sikora M., GASP-WEBT Consortium et al., 2012, *ApJ*, 751, 159
- Franceschini A., Rodighiero G., Vaccari M., 2008, *A&A*, 487, 837
- Gao S., Pohl M., Winter W., 2017, *ApJ*, 843, 109
- Gao S., Fedynitch A., Winter W., Pohl M., 2019, *Nat. Astron.*, 3, 88
- Ghisellini G., Maraschi L., Dondi L., 1996, *A&AS*, 120, 503
- Ghisellini G., Tavecchio F., Chiaberge M., 2005, *A&A*, 432, 401
- Giommi P., et al., 1999, *A&A*, 351, 59
- Guepin C., Kotera K., 2017, *A&A*, 603, A76
- H.E.S.S. Collaboration 2015, *ApJ*, 802, 65
- H.E.S.S. Collaboration 2019, *ApJ*, 870, 93
- Halzen F., Hooper D., 2005, *Astropart. Phys.*, 23, 537
- Halzen F., Kheirandish A., 2016, *ApJ*, 831, 12
- Halzen F., Zas E., 1997, *ApJ*, 488, 669
- Harrison F. A., et al., 2013, *ApJ*, 770, 103
- Hovatta T., Valtaoja E., Tornikoski M., Lähteenmäki A., 2009, *A&A*, 494, 527
- IceCube Collaboration 2013a, *Phys. Rev. Lett.*, 111, 021103
- IceCube Collaboration 2013b, *Science*, 342
- IceCube Collaboration 2014a, ([arXiv:1412.5106](#))
- IceCube Collaboration 2014b, *Phys. Rev. Lett.*, 113, 101101
- IceCube Collaboration 2015, *Astropart. Phys.*, 66, 39
- IceCube Collaboration 2016a, *JINST*, 11, P11009
- IceCube Collaboration 2016b, *Phys. Rev. Lett.*, 117, 241101
- IceCube Collaboration 2016c, *ApJ*, 833, 3
- IceCube Collaboration 2017b, in *Proceedings of ICRC 2017*. ([arXiv:1710.01179](#))
- IceCube Collaboration 2017a, in *Proceedings of ICRC 2017*. ([arXiv:1710.01191](#))
- IceCube Collaboration 2017c, *ApJ*, 835, 45
- IceCube Collaboration 2018, *Science*, 361, 147
- IceCube Collaboration 2019, *Eur. Phys. J.*, C79, 234
- IceCube Collaboration et al., 2018, *Science*, 361, eaat1378
- Inoue S., Takahara F., 1996, *ApJ*, 463, 555
- Inoue Y., Tanaka Y. T., 2016, *ApJ*, 828, 13
- James F., 1994, *MINUIT Function Minimization and Error Analysis: Reference Manual Version 94.1*
- James F., 2006, *Statistical methods in experimental physics*
- Jorstad S., Marscher A., 2016, *Galaxies*, 4, 47
- Jorstad S. G., et al., 2017, *ApJ*, 846, 98
- KM3NeT Collaboration 2009, *KM3NeT: Technical Design Report*
- Kadler M., et al., 2016, *Nature Phys.*, 12, 807
- Katz B., Waxman E., Thompson T., Loeb A., 2013. ([arXiv:1311.0287](#))
- Kaur N., Chandra S., Baliyan K. S., Sameer Ganesh S., 2017, *ApJ*, 846, 158
- Keivani A., et al., 2018, *ApJ*, 864, 84
- Krawczynski H., et al., 2004, *ApJ*, 601, 151
- Kuehr H., Witzel A., Pauliny-Toth I. I. K., Nauber U., 1981, *A&AS*, 45, 367
- Kushwaha P., et al., 2018a, *MNRAS*, 473, 1145
- Kushwaha P., et al., 2018b, *MNRAS*, 479, 1672
- Kushwaha P., de Gouveia Dal Pino E. M., Gupta A. C., Wiita P. J., 2019, in *Proceedings of BHCB 2018*. ([arXiv:1901.10768](#))
- Landoni M., Falomo R., Treves A., Scarpa R., Payá D. R., 2015, *ApJ*, 150, 181
- Liodakis I., Pavlidou V., 2015, *MNRAS*, 454, 1767
- Lister M. L., et al., 2019, *ApJ*, 874, 43
- Liu R.-Y., Wang K., Xue R., Taylor A. M., Wang X.-Y., Li Z., Yan H., 2019, *Phys. Rev.*, D99, 063008
- MAGIC Collaboration 2018, *ApJ*, 863, L10
- MAGIC Collaboration et al., 2015a, *MNRAS*, 450, 4399
- MAGIC Collaboration, VERITAS Collaboration, et al., 2015b, *A&A*, 578, A22
- MAGIC Collaboration, et al., 2017, *A&A*, 603, A31
- MAGIC Collaboration et al., 2018a, *MNRAS*, 480, 879
- MAGIC Collaboration et al. 2018b, *A&A*, 617, A30
- MAGIC Collaboration, et al., 2018c, *A&A*, 619, A45
- MAGIC Collaboration, FACT Collaboration, VERITAS Collaboration, et al., 2018d, *A&A*, 620, A181
- MAGIC Collaboration et al., 2019, *A&A*, 623, A175
- Manganaro M., et al., 2016, *Galaxies*, 4, 69
- Mannheim K., 1995, *Astropart. Phys.*, 3, 295
- Massaro E., Perri M., Giommi P., Nesci R., 2004, *A&A*, 413, 489
- Mücke A., Protheroe R. J., Engel R., Rachen J. P., Stanev T., 2003, *Astropart. Phys.*, 18, 593
- Murase K., Nagataki S., 2006, *Phys. Rev.*, D73, 063002
- Murase K., Takami H., 2009, *Astrophys.J.*, 690, L14
- Murase K., Waxman E., 2016, *Phys. Rev. D*, 94, 103006
- Murase K., Dermer C. D., Takami H., Migliori G., 2012a, *ApJ*, 749, 63
- Murase K., Beacom J. F., Takami H., 2012b, *JCAP*, 1208, 030
- Murase K., Inoue Y., Dermer C. D., 2014, *Phys. Rev. D*, 90, 023007
- Murase K., Guetta D., Ahlers M., 2016, *Phys. Rev. Lett.*, 116, 071101
- Murase K., Oikonomou F., Petropoulou M., 2018, *ApJ*, 865, 124
- Neronov A., Ribordy M., 2009, *Phys. Rev.*, D80, 083008
- Neronov A., Semikoz D. V., 2018. ([arXiv:1811.06356](#))
- Nilsson K., Pursimo T., Sillanpää A., Takalo L. O., Lindfors E., 2008, *A&A*, 487, L29

- Nilsson K., et al., 2018, *A&A*, **620**, A185
- O'Brien S., 2017, in Proceedings of ICRC 2017. ([arXiv:1708.02160](#))
- O'Brien S., 2018, *PoS*, ICRC2017, 650
- Oikonomou F., Murase K., Petropoulou M., 2019, in Proceedings of UHECR 2018. ([arXiv:1903.02006](#))
- Padovani P., Giommi P., 1995, *ApJ*, **444**, 567
- Padovani P., Resconi E., 2014, *Mon.Not.Roy.Astron.Soc.*, **443**, 474
- Padovani P., Resconi E., Giommi P., Arsioli B., Chang Y. L., 2016, *MNRAS*, **457**, 3582
- Padovani P., Giommi P., Resconi E., Glauch T., Arsioli B., Sahakyan N., Huber M., 2018, *MNRAS*, **480**, 192
- Padovani P., Oikonomou F., Petropoulou M., Giommi P., Resconi E., 2019, *MNRAS*, **484**, L104
- Paiano S., Landoni M., Falomo R., Treves A., Scarpa R., Righi C., 2017, *ApJ*, **837**, 144
- Paiano S., Falomo R., Treves A., Scarpa R., 2018, *ApJ*, **854**, L32
- Pakvasa S., Rodejohann W., Weiler T. J., 2008, *JHEP*, **02**, 005
- Palladino A., Rodrigues X., Gao S., Winter W., 2019, *ApJ*, **871**, 41
- Petropoulou M., Mastichiadis A., 2015, *MNRAS*, **447**, 36
- Petropoulou M., Dimitrakoudis S., Padovani P., Mastichiadis A., Resconi E., 2015, *MNRAS*, **448**, 2412
- Petropoulou M., Coenders S., Dimitrakoudis S., 2016, *Astropart. Phys.*, **80**, 115
- Pierre Auger Collaboration 2017, *JCAP*, **1704**, 038
- Plotkin R. M., Markoff S., Trager S. C., Anderson S. F., 2011, *MNRAS*, **413**, 805
- Rees M. J., 1967, *MNRAS*, **135**, 345
- Rees M. J., Meszaros P., 1992, *MNRAS*, **258**, 41P
- Reimer A., Boettcher M., Buson S., 2018. ([arXiv:1812.05654](#))
- Resconi E., 2019, to appear in Proc. XVIIIth International Workshop on Neutrino Telescopes
- Richards J. L., et al., 2011, *ApJS*, **194**, 29
- Righi C., Tavecchio F., Guetta D., 2017, *A&A*, **598**, A36
- Righi C., Tavecchio F., Inoue S., 2019, *MNRAS*, **483**, L127
- Rodrigues X., Fedynitch A., Gao S., Boncioli D., Winter W., 2018, *ApJ*, **854**, 54
- Rodrigues X., Gao S., Fedynitch A., Palladino A., Winter W., 2019, *ApJ*, **874**, L29
- Rosenfeld A. H., 1975, *Ann. Rev. Nucl. Part. Sci.*, **25**, 555
- STRAW Collaboration 2019, *JINST*, **14**, P02013
- Sbarrato T., Ghisellini G., Maraschi L., Colpi M., 2012, *MNRAS*, **421**, 1764
- Sbarrato T., Padovani P., Ghisellini G., 2014, *MNRAS*, **445**, 81
- Shi W., Liu X., Song H., 2007, *Ap&SS*, **310**, 59
- Smith P. S., Montiel E., Rightley S., Turner J., Schmidt G. D., Jannuzi B. T., 2009. ([arXiv:0912.3621](#))
- Stawarz L., Petrosian V., 2008, *ApJ*, **681**, 1725
- Stickel M., Padovani P., Urry C. M., Fried J. W., Kuehr H., 1991, *ApJ*, **374**, 431
- Sadowski A., Narayan R., 2015, *MNRAS*, **453**, 3213
- Tanaka Y. T., et al., 2016, *PASJ*, **68**, 51
- Tavecchio F., Ghisellini G., 2015, *MNRAS*, **451**, 1502
- Tavecchio F., Maraschi L., Ghisellini G., 1998, *ApJ*, **509**, 608
- Tavecchio F., Ghisellini G., Guetta D., 2014, *Astrophys.J.*, **793**, L18
- Tavecchio F., Oikonomou F., Righi C., 2019 ([arXiv:1906.02521](#))
- Torres-Zafra J., Cellone S. A., Buzzoni A., Andruchow I., Portilla J. G., 2018, *MNRAS*, **474**, 3162
- Tramacere A., Massaro F., Cavaliere A., 2007, *A&A*, **466**, 521
- Tsujimoto S., et al., 2017, in Proceedings of ICRC 2017. ([arXiv:1709.05063](#))
- Turley C. F., et al., 2016, *ApJ*, **833**, 117
- Turley C. F., Fox D. B., Keivani A., DeLaunay J. J., Cowen D. F., Mostafa M., Ayala Solares H. A., Murase K., 2018, *ApJ*, **863**, 64
- Urry C. M., Padovani P., 1995, *Publ. Astron. Soc. Pac.*, **107**, 803
- VERITAS Collaboration 2003, *ApJ*, **583**, L9
- VERITAS Collaboration 2005, *ApJ*, **621**, 181
- VERITAS Collaboration 2018, *Astrophys. J.*, **861**, L20
- VERITAS Collaboration, Böttcher M., Fumagalli M., 2014, *ApJ*, **797**, 89
- Valtonen M. J., et al., 2006, *ApJ*, **643**, L9
- Wang K., Liu R.-Y., Li Z., Wang X.-Y., Dai Z.-G., 2018. ([arXiv:1809.00601](#))
- Waxman E., 1995, *ApJ*, **452**, L1
- Yuan C., Murase K., MÅł'szÅąros P., 2019. ([arXiv:1904.06371](#))

APPENDIX A: FLARE DEFINITION

There is no unambiguous definition of blazar flaring states. In this work, in order to homogeneously define the flare periods we used the FAVA data ([Fermi-LAT Collaboration 2017](#)). We consider only the high-energy FAVA energy bin (> 800 MeV) to limit the uncertainties introduced to our results by the larger point spread function of the *Fermi*-LAT at low energies. We look for flaring activity in the FAVA data, during the flares as defined in Table 1. As a reminder, the flares were selected in several different wavebands. In FAVA, we define the flare period, as the two-tailed, gaussian, one-sigma region around the mean. In addition to obtaining the flare period for each of the flares studied in the earlier sections, we identify further periods of strong flux enhancement in the FAVA light-curves of the sources in our sample. We consider all periods during which flaring activity was observed, at the $\geq 5\sigma$ level, according to the standard FAVA definition. The FAVA significance definition, which examines the Poisson deviation of each bin with respect to the expected background counts, is most sensitive to sharply peaked variations of the flux. We therefore, also identify, longer but less sharply peaked flux enhancements visually, and fit them with a gaussian function to obtain their respective durations. Each of these selected periods typically contain one or more $\geq 4\sigma$ upward fluctuations. The FAVA lightcurves, and fitted flares are shown in Figure A1. The data are binned in photon counts detected per week, N_γ , and are plotted as relative fluxes, $(N_\gamma - N_{\gamma,av})/N_{\gamma,av}$, with, $N_{\gamma,av}$, the expected number of background photons per week. For some sources (TXS 0506+056, S5 0716+714, OJ 287, S2 0109+22, Mrk 501, Mrk 421, BL Lac, AO 0235+164, 3C 66A) the baseline $N_{\gamma,av}$ given by FAVA needed slight adjustment to obtain relative fluxes of zero in non-flaring time periods. Changes of baseline in the FAVA lightcurves, where observed, are generally related to a change in the background model caused by, for example, changes in the *Fermi*-LAT observing mode over time.

Blue triangles denote weeks during which there was flaring activity at the $\geq 5\sigma$ level according to the FAVA definition. Green triangles denote the mean of our canonical flare periods studied in the earlier sections. We present combined fits to the entire light-curves, which sometimes identify periods of low plateaus of enhanced activity. For TXS 0506+056 the green dashed lines give the duration of the 2014-2015 neutrino flare. The green solid line gives the time of detection of IC170922A. For AO 0235+164 the solid green vertical line gives the time of the GFU neutrino alert.

Table 5 gives the estimated flare durations based on the

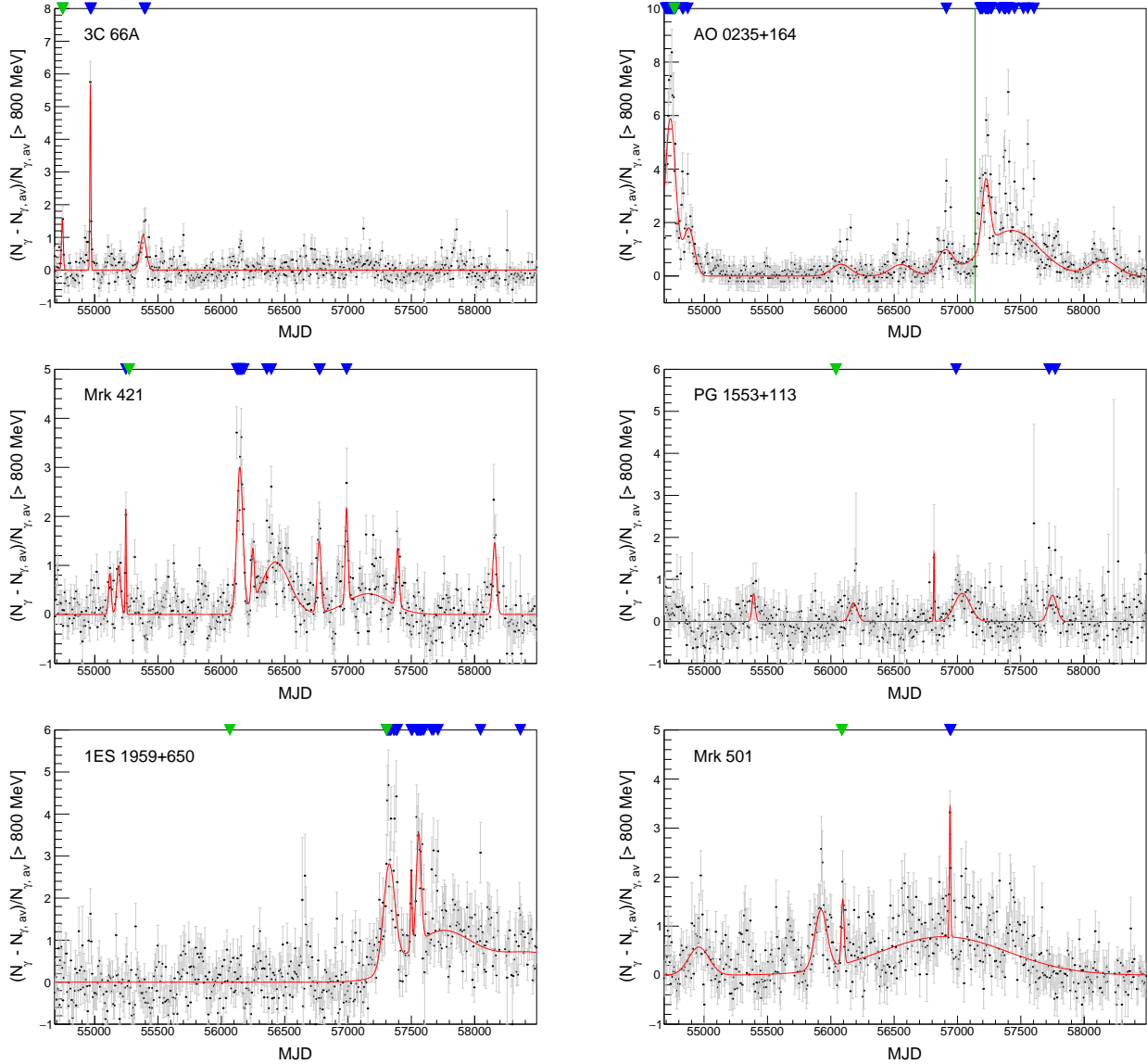


Figure A1. FAVA lightcurves and fitted flares. Blue triangles mark the times when the FAVA lightcurves exhibit a $\geq 5\sigma$ flare in the high-energy FAVA bin. In the case of PG 1553+113, which did not exhibit any $\geq 5\sigma$ flares, the $\geq 4\sigma$ flares are shown instead. Green triangles mark the time of the flare(s) modelled in the present work. For AO 0235+164 the solid green vertical line gives the time of the GFU neutrino alert.

analysis of the FAVA lightcurves, or in the absence of significant flux enhancement in the FAVA data, the flare timescale determined in a different waveband as stated. The table also gives the timescale of smallest detected time-variability in days, $t_{\text{var,Obs,d}}$, which we use to determine the size of the emitting region and waveband at which it was detected. Since the FAVA data are by default weekly binned we used the shortest variability available at any wavelength to determine $t_{\text{var,Obs,d}}$. Source by source details are given below.

- For 3C 66A the studied flare was seen with $> 5\sigma$ significance in the HE FAVA data over a period of two-weeks. A coincident flare with similar duration was seen in the optical data. A shorter flare was seen in the VHE γ -ray data.
- For AO 0235+164 the FAVA data show an ~ 84 -day long high state in August 2008, soon after the launch of *Fermi*,

consistent with the γ -ray analysis of [Fermi-LAT Collaboration, et al. \(2012\)](#), followed by a lower-intensity second flare. We have additionally identified a long, γ -ray flare in 2015 as potentially interesting from the point of view of neutrino production as discussed in Section 4.

- For Mrk 421 the FAVA data show no significant flare, though as reported in earlier analyses ([MAGIC Collaboration, et al. 2015b](#); [Petropoulou et al. 2016](#)) the X-ray and VHE activity were remarkable. We therefore assume the VHE flare timescale for the present analysis.

- In the case of PG 1553+113, no 5σ flares were recorded by the FAVA analysis. We nevertheless, flag the $\geq 4\sigma$ flares for this source. The April 2012 flare does not appear as a period of significant enhancement in the FAVA data. We thus assume a 30-day duration, as measured with the *Swift*-XRT,

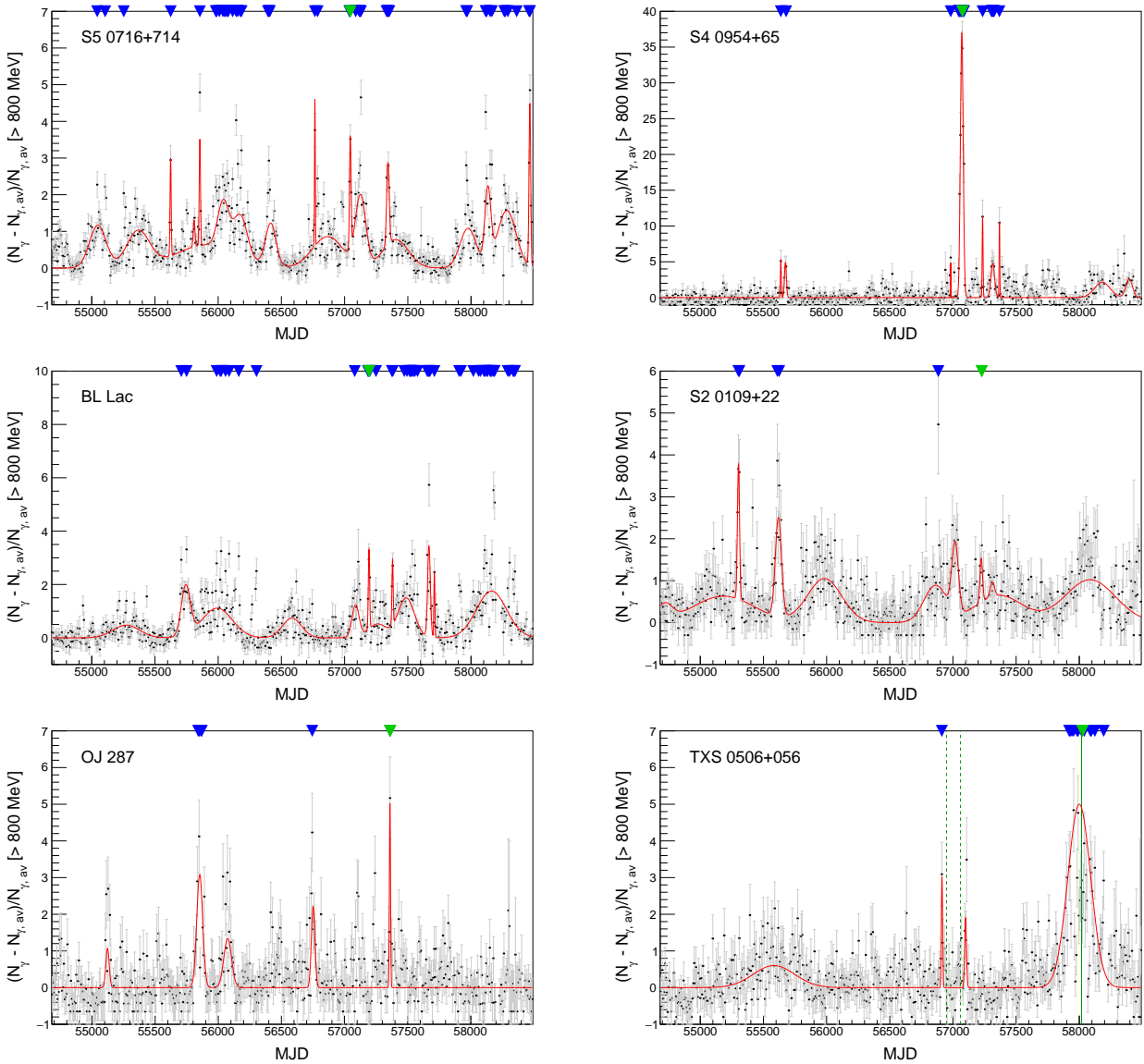


Figure A1 – *continued* FAVA lightcurves and fitted flares. For TXS 0506+056 the green dashed lines give the duration of the 2014-2015 neutrino flare. The green solid line gives the time of detection of IC170922A.

noting that the 6-day VHE flare observed with MAGIC preceded the flare in the X-ray data.

- For 1ES 1959+650 the May 2012 flare does not coincide with any flaring activity in FAVA. In the VHE γ -ray data there was a short-lived flare on May 20th 2012 (MJD 57067), and the X-ray data showed an enhancement approximately one week later. The optical data showed a historically high-state between MJD 57034 and MJD 57080. The optical, and UV flux did not change much during this entire period. We thus use the optical/UV duty cycle in the present analysis. For the October 2015 outburst of 1ES 1959+650, an 84-day long, high-significance flare is seen in the FAVA data, consistent with the analysis of [Kaur et al. \(2017\)](#). Several flares follow and the source remains in a higher than average state until the end of the available FAVA data.

- For Mrk 501 the VHE flare was preceded by a flare at X-ray wavelengths by a few days, but the optical and low-

energy data show no significant flux enhancement. A low significance ~ 21 -day flare ($\sim 2.5\sigma$) level can be identified in the HE FAVA data, which defines the timescale used for the present analysis.

- For S5 0716+714 a ~ 2 week long, $> 5\sigma$ flare is seen in the FAVA data. Coincident flux enhancements were seen at other wavelengths including X-ray and optical and VHE γ -ray observations.

- The flares of S4 0954+65 are short and very intense with respect to the flares of the other sources in our sample, in general. During the February 2015 flare, the relative flux increased by as much as a factor of ~ 40 in the HE FAVA data.

- Multiple short flares can be seen in the FAVA data of BL Lac during June 2015. The VHE flare seen by MAGIC coincides with a ~ 7 -day strong FAVA flare, which we assume as the relevant timescale in our analysis.

Table B1. Abbreviations and acronyms used in this article.

GVD	Baikal Gigaton Volume Detector
Gen2	IceCube-Gen2: The proposed extension of the IceCube detector
IC40	Partial IceCube configuration April 5 2008 - May 20 2009
IC59	Partial IceCube configuration May 20 2009 - May 31 2010
IC79	Partial IceCube configuration May 13 2010 - May 16 2011
IC86	Partial IceCube configuration May 16 2011 - to date
KM3NeT	Cubic Kilometre Neutrino Telescope
ONC	Ocean Networks Canada

- For S20109+22, the 2015 studied flare, does not coincide with as strong flare in the HE FAVA data. There is an enhancement at the 2σ level, over a period of ~ 21 days, consistent with the report of the *Fermi* analysis of [MAGIC Collaboration et al. \(2018a\)](#), who confirm a flux doubling with respect to the baseline 3FGL flux during this period. We use this estimate for the flare duration.

- The December 2015 flare of OJ287 coincides with a week long enhancement in the HE FAVA data at the 5σ level. In other wavelengths, several flares were seen until the source returned to its pre-outburst state in May 2016. In addition, the source reached a historic maximum in the X-ray band in February 2017. It was followed up and observed in several wavelengths, and it was possible to detect it in the VHE band for the first time with VERITAS ([O’Brien 2018](#)). This second enhancement was not visible in the FAVA data and has not been modelled here.

- The 2017 flare of TXS0506+056 in the FAVA data can be well described by a gaussian peaked at MJD58000 and duration 175 days. Our estimate is in agreement with the results of [IceCube Collaboration et al. \(2018\)](#).

APPENDIX B: TABLE OF ACRONYMS

Table B1 gives the definition of abbreviations and acronyms used in this article.